Journal Pre-proof

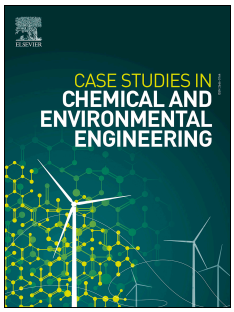

Composite Adsorbent from Sugarcane (*Saccharum officinarum*) Bagasse Biochar Generated from Atmospheric Pressure Microwave Plasma Pyrolysis Process and Nano Zero Valent Iron (nZVI) for Rapid and Highly Efficient Cr(VI) Adsorption

Denny Dermawan, Aulia Diva Satriavi, Dyah Isna Nurhidayati, Rahmad Firnandi, Novi Eka Mayangsari, Tarikh Azis Ramadani, Dika Rahayu Widiana, Anda Iviana Juniani, Dwi Rasy Mujiyanti, Ya-Fen Wang

PII: S2666-0164(25)00030-1

DOI: https://doi.org/10.1016/j.cscee.2025.101123

Reference: CSCEE 101123

To appear in: *Case Studies in Chemical and Environmental Engineering*

Received Date: 30 November 2024

Revised Date: 23 January 2025

Accepted Date: 26 January 2025

Please cite this article as: D. Dermawan, A.D. Satriavi, D.I. Nurhidayati, R. Firnandi, N.E. Mayangsari, T.A. Ramadani, D.R. Widiana, A.I. Juniani, D.R. Mujiyanti, Y.-F. Wang, Composite Adsorbent from Sugarcane (*Saccharum officinarum*) Bagasse Biochar Generated from Atmospheric Pressure Microwave Plasma Pyrolysis Process and Nano Zero Valent Iron (nZVI) for Rapid and Highly Efficient Cr(VI) Adsorption, *Case Studies in Chemical and Environmental Engineering*, https://doi.org/10.1016/j.cscee.2025.101123.

Composite Adsorbent from Sugarcane (*Saccharum officinarum*) Bagasse Biochar Generated from Atmospheric Pressure Microwave Plasma Pyrolysis Process and Nano Zero Valent Iron (nZVI) for Rapid and Highly Efficient Cr(VI) Adsorption

Denny Dermawan [1,3]*, Aulia Diva Satriavi[1], Dyah Isna Nurhidayati[1], Rahmad Firnandi[1], Novi Eka Mayangsari[1,3], Tarikh Azis Ramadani[1,3], Dika Rahayu Widiana[2], Anda Iviana Juniani[4], Dwi Rasy Mujiyanti[5,6], Ya-Fen Wang[5,6]

[1]Waste Treatment Engineering Study Program, Shipbuilding Institute of Polytechnic Surabaya, Jalan Teknik Kimia, Kampus ITS Sukolilo, Surabaya, Indonesia

[2]Safety and Risk Engineering Study Program, Shipbuilding Institute of Polytechnic Surabaya, Jalan Teknik Kimia, Kampus ITS Sukolilo, Surabaya, Indonesia

[3]Waste Treatment Engineering Laboratory, Shipbuilding Institute of Polytechnic Surabaya, Jalan Teknik Kimia, Kampus ITS Sukolilo, Surabaya, Indonesia

[4]Design and Manufacture Study Program, Shipbuilding Institute of Polytechnic Surabaya, Jalan Teknik Kimia, Kampus ITS Sukolilo, Surabaya, Indonesia

[5]Department of Environmental Engineering, Chung Yuan Christian University, Chung-Li, 320, Taiwan

[6]Center for Environmental Risk Management, Chung Yuan Christian University, Chung-Li, 32023, Taiwan

*Corresponding author:

Denny Dermawan, PhD (denny.dermawan@ppns.ac.id)

Abstract

Sugarcane bagasse, with a 25–28% lignin content, can be converted into biochar, serving as a promising adsorbent due to its high surface area. Nano-zero-valent iron (nZVI) is known for its strong magnetization and ability to bind heavy metals. In this research, biochar derived from sugarcane bagasse was composited with nZVI at varying ratios (1:1, 2:1, and 3:1) to improve adsorption efficiency for Cr (VI) removal. The composites were synthesized using the biochar from the plasma pyrolysis method, followed by nZVI incorporation. Batch adsorption tests were conducted with different Cr (VI) concentrations, contact times, pH levels, and adsorbent doses to determine the optimum conditions for each ratio. Characterization of the adsorbent included XRD, BET, FTIR, SEM, VSM, and Zeta potential analysis. XRD analysis of sugarcane bagasse and biochar demonstrated crystallinity and particle size improvements post-pyrolysis. BET results showed that sugarcane bagasse biomass had a surface area of 0.061 m^2/g, which increased to 87.50 m^2/g after conversion to biochar. However, once composited with nZVI, the surface area decreased to 37.44 m^2/g (1:1), 49.26 m^2/g (2:1), and 62.37 m^2/g (3:1). FTIR and SEM analyses revealed the interactions between biochar and nZVI, as well as the binding of Cr (VI) to the composite surfaces. VSM showed a reduction in magnetization after adsorption, confirming the oxidation of nZVI to various iron oxides (e.g., FeO, Fe_2O_3, Fe_3O_4), which are less magnetic. The adsorption tests indicated that the adsorption capacity increased with a higher SBB/nZVI ratio. The biochar alone had an adsorption capacity of 77.82 mg/g. In comparison, the composites achieved 86.47 mg/g (1:1), 95.12 mg/g (2:1), and 112.41 mg/g (3:1). Optimal removal was achieved at an initial Cr (VI) concentration of 175 mg/L, a contact time of 180 minutes, and a pH of 2. The Langmuir isotherm model best described the adsorption behavior, and the adsorption kinetics followed a pseudo-second-order model, indicating chemisorption as the primary mechanism. The study concluded that the composite's adsorption efficiency increased with a higher nZVI ratio, making the 3:1 ratio the most effective for Cr (VI) removal.

Keywords: Atmospheric Pressure Microwave Plasma, Pyrolysis, Sugarcane Bagasse Biochar, Nano Zero Valent Iron, Cr (VI) removal.

1. Introduction

One of the most dangerous heavy metals to the environment is hexavalent chromium Cr(VI). Cr(VI) accumulates in soil and wastewater, posing risks to human health and the environment [1]. Chronic inhalation of Cr(VI) can lead to respiratory symptoms like septal perforation, ulcers, bronchitis, lung dysfunction, pneumonia, and nose irritation. Chronic inhalation or oral exposure to high levels of Cr(VI) can adversely affect the liver, kidneys, gastrointestinal tract, blood, and immune system. Its high oxidation capacity is associated with its toxicity, potentially leading to cell death [2,3].

The tanning industry is a significant source of Cr(VI) contamination, as chromium salts used in tanning methods account for about 90% of leather produced globally [4,5]. Through cross-linking agents, tanning stabilizes the skin's collagen matrix against microbial degradation [6]. However, only about 60% of the chromium tanning agents are absorbed by the leather, with the remainder leading to waste [5,7,8]. The leather tanning industry has seen increased production, with Indonesia's GDP reaching Rp 7.57 trillion in Q2 2022, a 13.12% increase compared to the previous year. Waste from the tanning industry contains harmful substances like sulfides, ammonia, acids, and chromium. Wastewater from tanning contains about 49 mg/L of chromium, while Indonesia’s environmental regulations mandate that total chromium in wastewater from tanning industries must not exceed 0.6 mg/L [9].

Biochar has garnered significant attention because it offers various functional groups, high porosity, and a large specific surface area at a relatively low cost, fulfilling economic and environmental requirements [10]. Biochar can be made from biomass waste, such as rice husks, jengkol shells, and sugarcane bagasse [11]. Sugarcane bagasse is a low-cost, renewable lignocellulosic biomass residue obtained after crushing sugarcane. It contains 25-28% lignin, 61-63% carbohydrates, 5-6% extractives, and 6-7% ash [12]. Indonesia produces large amounts of sugarcane (*Saccharum officinarum*), reaching 33,000,000 tons/year, with 11,220,000 tons of bagasse waste/year [13]. One ton of sugarcane yields approximately 115 kg of sugar, around 300 kg of bagasse, and other by-products like filter cake, molasses, and furnace ash [14]. Biochar from sugarcane bagasse has been shown to reduce heavy metals such as nickel [15], lead [16], copper, cadmium [17], and chromium [18]. Carbonization can produce biochar, which is divided into oxidation, gasification, and pyrolysis. Oxidation is an industrial process where organic material is transformed into carbon through destructive distillation. At the same time, gasification converts carbon-containing products into gas by heating them in a low-oxygen environment. Conversely, pyrolysis decomposes organic materials without oxygen, producing biochar, tar, and gas products. Numerous single-process biochars were generated using conventional indirect heating

in a furnace. However, conventional pyrolysis or gasification of waste biomass generally yields biochar with low pore characteristics compared to commercial activated carbon [19].

Plasma technology is one of the methods used in pyrolysis, offering advantages like rapid heating, high temperatures, and smaller plant installations compared to conventional indirect heating [20]. Plasma technology, an advanced thermochemical process, has garnered considerable attention for its efficacy in processing various biomass as an advanced pyrolysis process that could produce high-quality biochar [19]. Atmospheric pressure microwave plasma, one of the plasma pyrolysis methods, generates an electrical arc that transforms electrical energy into thermal energy. Subsequently, ionization transforms plasma gas into conductive materials and induces disassociation, excitation, detachment, attachment, and molecule and atomic transfer, all contributing to component disintegration [21]. The advantages of plasma technology encompass direct and rapid heating, elevated temperatures, a more compact installation footprint, and a greater variety of chemical operations than conventional indirect heating in a furnace. The interaction between reactive species and biomass in the plasma machine can augment the surface area of biochar and facilitate the incorporation of carboxyl (–COOH), carbonyl (–CO), and hydroxyl (–OH) groups on the material surface, thereby markedly enhancing the adsorption capacity. However, there is only a limited number of research regarding the application of plasma technology for biochar production.

Nano zero-valent iron (nZVI) has gained popularity in wastewater treatment due to its reduction potential, reactivity, and cost-effective production process [22]. nZVI is commonly used to treat pollutants in groundwater and facilitates groundwater remediation. The advantages of using nZVI include low cost, high specific surface area, and excellent reactivity [23, 24, 25]. However, the application of nZVI technology in contaminant adsorption still faces limitations, such as nZVI particle agglomeration [26]. Nano-scale iron particles tend to attract each other and form larger aggregate particles, significantly reducing their specific surface area and reduction capacity [26,27]. Agglomeration in nZVI can be mitigated by compositing it with other materials. Various materials used in nZVI composites include bentonite [28], mesoporous silica [29], kaolinite [30], sepiolite [31], activated carbon [32], and biochar [33].

Previous research showed that biochar, activated carbon, and nZVI could remove Cr(VI). Dew melon peel biochar had an adsorption capacity of 98.6 mg/g with 100 mg/L of Cr(VI) [34]. Then, sugarcane bagasse biochar had an adsorption capacity of 80.6 mg/g with 100 mg/L of Cr(VI) [35]. Ricestraw-activated carbon had an adsorption capacity of 29.34 mg/g with 30 mg/L of Cr(VI). nZVI itself could remove Cr(VI) with an adsorption capacity of 27.8

mg/g with 45 mg/L of Cr(VI). Biochar composited with nZVI exhibited high stability and excellent degradation performance for various pollutants [10]. However, there is no research on applying plasma technology for biochar production and synthesizing it with nZVI to remove Cr(VI) from wastewater.

To the author's best knowledge, no research has been conducted on composite adsorbents utilizing biochar produced from atmospheric pressure microwave plasma synthesized with nZVI. This study addresses environmental remediation by utilizing secondary raw materials, specifically, sugarcane bagasse-derived biochar composited with nZVI, for efficient Cr(VI) removal. Plasma pyrolysis, an underexplored biomass carbonization method, enhanced surface properties compared to traditional pyrolysis techniques. This research used a biochar/nZVI composite adsorbent, assessing the impact of operational parameters such as initial Cr(VI) concentration, contact time, adsorbent dosage, and pH. Adsorption data were analyzed using isotherm models to understand the mechanism. Characterization was conducted using Scanning Electron Microscope (SEM), X-ray diffraction (XRD), Fourier Transform Infrared Spectroscopy (FTIR), Brunauer-Emmett-Teller (BET) analysis, Vibrating Sample Magnetometry (VSM), and Zeta Potential, providing a comprehensive evaluation of the adsorbent's morphology, crystallinity, surface area, magnetization, and surface charge.

2. Material and methods

2.1. Preparation of Sugarcane Bagasse Biochar

Preparing raw samples involved boiling the sugarcane bagasse (SB) (Figure S1) in water. Subsequently, the SB was meticulously chopped into smaller pieces and dried in an oven at 80°C for 4 hours. Once completely dried, the samples were placed in a ball mill to be crushed and sifted through a 100-mesh sieve.

The pyrolysis process commenced by placing the prepared samples into the plasma machine. The plasma was activated with two independent gas flow channels set to 9 L/min for 5 minutes. The microwave input power was maintained at 1.2 kW, under a nitrogen gas pressure of 30 psi, and at 300°C. Following the process, the produced biochar (Figure S1) was stored in airtight containers to prevent potential degradation or contamination.

2.2. Preparation of Nano-Zero-Valent Iron (nZVI)

The synthesis of Nano Zero-Valent Iron (nZVI) involved combining 1 gram of sodium borohydride ($NaBH_4$, molecular mass: 37.83 g/mol, Merck, 99% purity) with 10 grams of iron(II) sulfate heptahydrate ($FeSO_4 \cdot 7H_2O$, molecular mass: 278.02 g/mol, Merck, 99% purity) under a nitrogen atmosphere to prevent oxidation during the

process. $NaBH_4$ was initially dissolved in 25 mL of distilled water, while $FeSO_4 \cdot 7H_2O$ was diluted in 150 mL of distilled water and 100 mL of ethanol. The formation of nZVI occurred by gradually adding the $NaBH_4$ solution to the $FeSO_4 \cdot 7H_2O$ mixture while continuously stirring. The change in color of the aqueous solution, which progressively darkens to black, served as an observable indicator of the reaction's progression.

2.3. Preparation of Sugarcane Bagasse Biochar (SBB)/Nano-Zero-Valent Iron (nZVI) Composite

The synthesis of the composites followed distinct procedures. The SBB/nZVI composite adsorbent (Figure S2) was prepared in a single step by incorporating biochar during the nZVI formation process, followed by submerged into ethanol for storage. The ratio of SBB to nZVI is 1:1, 2:1, and 3:1.

2.4. Adsorption Experiment of Composite on Cr(VI) Solution

2.4.1. Effect of pH

This testing was conducted using potassium dichromate ($K_2Cr_2O_7$, molecular mass: 294.18 g/mol, Merck, 99% purity) with a volume of 50 mL of Cr (VI) solution with a concentration of 175 mg/L was added, and the pH was adjusted to various levels, including 2, 4, 6, 8, 10, and 12, using the addition of 0.1 M hydrochloric acid (HCl, diluted from 37% HCl solution, molecular mass: 36.46 g/mol, Merck) or 0.1 M sodium hydroxide (NaOH, molecular mass: 40.00 g/mol, Merck, 99% purity). The SBB/nZVI adsorbent composition ratios used were 1:1, 2:1, and 3:1. The adsorbent dosage, contact time, and stirring speed used in each adsorption process were 1 g/L, 180 minutes, and 150 rpm, respectively. The mixture that reached the specified contact time was then filtered using filter paper (Whatman No. 41 Filter Paper), and the filtrate was analyzed using a UV-Vis spectrophotometer (Agilent Cary 60) at a wavelength of 665 nm. The experimental results were the mean values of the triplicated Cr(VI) adsorption experiments. The adsorption capacity was calculated using equation (1) as follows:

$$Q_t = \frac{C_o - C_t}{W} V \quad (1)$$

where Q_t is the adsorption capacity of Cr (VI) (mg/g) at t minutes. C_o and C_t, respectively, represent the initial concentration and concentration at t (mg/L).

2.4.2. Effect of Initial Concentration and Contact Time

A total of 50 mL of Cr (VI) solution with varying initial concentrations of Cr (VI) solution at 25, 50, 75, 100, 125, 150, and 175 ppm. The SBB/nZVI adsorbent composition ratio used was 1:1, 2:1, and 3:1. The adsorbent dosage, solution pH, and stirring speed used in each adsorption process were 1 g/L, 2, and 150 rpm, respectively. Furthermore, the adsorption process was conducted in batch mode with a contact time of 30, 60, 90, 120, 150, and 180 minutes. Furthermore, the mixture was filtered using filter paper, and the filtrate was analyzed using a UV-Vis spectrophotometer to determine the residual concentration of Cr (VI).

2.4.3. Effect of Adsorbent Dosage

A volume of 50 mL of Cr (VI) solution with a concentration of 175 mg/L was added. The process was then continued with the addition of adsorbent with varying dosages of 0.2, 0.6, and 1 g/L at SBB/nZVI adsorbent compositions of 1:1, 2:1, and 3:1. The contact time, solution pH, and stirring speed used in each adsorption process were 180 minutes, 2, and 150 rpm, respectively. The mixture was then filtered using filter paper, and the filtrate was analyzed using a UV-Vis spectrophotometer to determine the residual concentration of Cr (VI).

2.5. Adsorption Isotherm

The commonly used adsorption isotherm models in the adsorption process were the Langmuir, Freundlich, Temkin, and Dubinin-Radushkevich equations [36]. These isotherm equations were used to analyze the adsorption mechanism of Cr (VI) on the used adsorbent. Determination of the type of isotherm was carried out by plotting linear regression curves. Isothermal adsorption analysis was conducted for the composite adsorbent ratios of 1:1, 2:1, and 3:1, with varying initial Cr (VI) of 25-175 ppm, using a dose of 1 g/L. The adsorbent with a predetermined dose was then contacted with a Cr (VI) solution at normal temperature until it reached equilibrium. The Langmuir model defined that the maximum adsorption capacity occurred due to the formation of a monolayer of adsorbate on the adsorbent surface. Meanwhile, the Freundlich isotherm lacked the ability to predict the presence of sites on the surface that could prevent further adsorption as equilibrium was reached. This showed that only a few active sites were capable of adsorbing dissolved molecules. The Temkin isotherm indicates that the heat of adsorption decreases linearly as the extent of adsorption increases. This model is temperature-dependent and pertains to the interactions between the adsorbate and the adsorbent surfaces, involving all molecules within the adsorption layer. The adsorption liquid state is intricate due to the disordered arrangement of adsorbed molecules, which are neither uniformly organized nor firmly packed. The Dubinine-Radushkevich isotherm model elucidates the porous structure of the adsorbent. This concept is

predicated on the adsorption potential theory, which posits that adsorption transpires by the incorporation of microporous adsorbate into the adsorbent rather than adhering to the pore walls.

The Langmuir (Eq. (2)), Freundlich (Eq. (3)), Temkin (Eq. (4)), and Dubinine Radushkevich (Eq. (5) & (6)) adsorption isotherm equations were as follows [37,38]:

$$\frac{C_e}{Q_e} = \frac{1}{Q_m K_L} + \frac{C_e}{Q_m} \quad (2)$$

$$\mathrm{Log}Q_e = \log K_f + \frac{1}{n}\log C_e \quad (3)$$

$$q_e = \frac{Rt}{bt}\ln a_t + \frac{Rt}{bt}\ln C_e \quad (4)$$

$$\ln Q_e = \ln Q_m - B\varepsilon^2 \quad (5)$$

$$\varepsilon = RT\ln\left(1 + \frac{1}{C_e}\right) \quad (6)$$

where Q_m is the monolayer adsorption capacity (mg/g), and K_L is the Langmuir equilibrium constant (L/mg). K_f and n are Freundlich constants related to adsorption capacity and intensity of adsorption, t (K) is the ambient temperature of the adsorption process, R is the ideal gas constant (8.314 J mol^{-1} K^{-1}), b_t (J/mol) are Temkin isotherm constants attributed to the adsorption heat, and a_t (L/g) is the Temkin isotherm equilibrium binding constant, B is the adsorption energy constant (mol^2/J^2), Qe and Qm (mg/g) are the adsorption capacity and the maximum adsorption capacity of the composite adsorbent, ε is the Polanyi potential, and T is the ambient temperature (K). C_e represents the equilibrium concentration of the adsorbate in the solution (mg/L), calculated using the following equation (7):

$$Q_e = \frac{C_o - C_e}{W} V \quad (7)$$

where Q_e is the adsorption capacity of Cr (VI) at equilibrium conditions (mg/g).

2.6. Adsorption Kinetic

The experimental results at various contact times, reflecting alterations in the quantity of Cr(VI) adsorbed, were analyzed to evaluate the kinetic adsorption of Cr(VI) onto the composite adsorbent surface and subsequently fitted into four further kinetic models. The pseudo-first-order model (Eq. (8)), pseudo-second-order model (Eq. (9)), intra-

particle diffusion model (Eq. (10)), and Elovich model (Eq. (11)) were utilized and articulated as the following equations to assess the kinetic data [37; 38]:

$$\ln(q_e - q_t) = \ln q_e - k_1 t \quad (8)$$

Where q_e = adsorption capacities at equilibrium (mg/g); q_t = adsorption capacities at time t (mg/g); k_1 = Pseudo-first-order rate constant (min^{-1}).

$$\frac{t}{q} = \frac{1}{k_2 q_e^2} + \frac{t}{q_e} \quad (9)$$

The pseudo-second-order rate constant is k_2, and the other symbols have the same meaning as described in the above equation. A plot of t/q vs. t gives a linear line for this order-compliant kinetics. The slope from the given linear equation is $\frac{1}{q_e}$ and the intercept is $\frac{1}{k_2 q_e^2}$.

$$q_t = k_{int} t^{0.5} + B \quad (10)$$

The intra-particle diffusion rate constant is kint, and B is the initial adsorption (mg/g). A plot of q_t and $t^{0.5}$ gives a linear line to an adsorption process that is compliant with it, and its slope is k_{int}.

$$q_t = \frac{1}{\beta} \ln(\propto \beta) + \frac{1}{\beta} \ln t \ \ln \quad (11)$$

2.7. Material Characterization

The morphological analysis of activated biomass, biochar, and composite before and after adsorption was performed using Scanning Electron Microscopy (SEM; type FEI Inspect S50), operated at 20 KV. The chemical structure showing functional groups was analyzed using Fourier Transform Infrared (FTIR spectroscopy; type Nicolet

iS10) within the wavenumber range of 4000-500 cm^{-1}. The specific surface area, pore size, and pore volume of the material were determined using the Brunauer-Emmett-Teller (BET method; Quantachrome Nova 2000E). The material's crystallinity and phase composition degree were assessed using X-ray diffraction (XRD analysis, PANalytical X'Pert type), operated at 30 mA and 40 KV. The magnetization range was assessed using Vibrating Sample Magnetometry (VSM analysis; type Cryogen-free 3 Tesla). The surface charge and composite adsorbent size were detected by zeta potential analysis (Zetasizer Nano ZS; Malvern Inc., UK).

3. Results and discussions

3.1. XRD

The diffraction peak patterns from XRD testing were used to analyze the crystallinity of biomass, biochar, and biochar from SB modified with nano zero-valent iron (nZVI), referencing JCPDS 09-0432. Figure 1 presents the XRD diffractogram patterns, providing crucial insights into the physicochemical transformations occurring during thermal treatment and subsequent nZVI modification relevant to environmental remediation applications. Initially, the XRD pattern of untreated biomass displays broad and less intense peaks at 29.8° and 35.3°, indicative of its primarily amorphous structure interspersed with crystalline mineral inclusions [39]. Upon thermal conversion to biochar, these peaks sharpen and shift slightly to 29.9° and 35.1°, suggesting enhanced crystallinity, possibly due to the thermal decomposition of organic components and crystallization of inorganic minerals. Table 1 shows a slight shift in the main peak position from 35.3° (biomass) to 35.1° (biochar). The crystallinity index, calculated by the Segal method, shows that biomass has a higher index (15.58%) than biochar (14.81%), suggesting biochar contains more amorphous material due to crystalline region degradation during pyrolysis [40].

The crystallite size differs, with biomass at 16.66 nm and biochar at 16.67 nm, indicating an increase in crystallite size for biochar. This suggests thermal rearrangement and recrystallization of carbon structures during pyrolysis. These structural changes have significant implications for biochar's adsorption properties. The higher amorphous content and larger crystallite size in biochar suggest an increase in surface area and active sites, which enhances biochar's capacity to absorb contaminants. Additionally, larger crystalline domains may provide a stable framework that supports the porous structure, improving biochar's mechanical stability and durability as an adsorbent [39, 41].

Subsequent modification with nZVI introduces distinct new peaks at 30.5° and 44.0°, corresponding to the (220) and (110) planes of hematite (Fe_2O_3) and metallic iron (Fe^0), respectively. This confirms the successful incorporation

of iron phases within the biochar matrix, which is crucial for its intended use in pollutant adsorption and reduction. Post-adsorption, the XRD patterns of biochar/nZVI exhibit minor variations in peak intensity, possibly reflecting interactions between the iron compounds and adsorbed pollutants, altering their chemical and physical interface. The broadening of peaks in the XRD diffractogram for biochar/nZVI, especially noted before and after adsorption, indicates smaller particle sizes of nZVI. This observation is crucial for environmental applications because smaller nanoparticles have a larger specific surface area relative to their volume. This increased surface area enhances the reactivity of nZVI towards contaminants [42].

These structural insights, revealed through XRD analysis, are critical for understanding the mechanisms underlying the enhanced reactivity and stability of nZVI-modified biochar in environment applications. The ability of this composite material to adsorb and reduce pollutants is likely influenced by the nano-scale dispersion of reactive iron phases within the biochar structure, which can interact effectively with contaminants. Such materials are proving invaluable in the remediation of polluted environments, offering a sustainable approach to managing industrial waste and improving ecological outcomes.

3.2. FTIR

FTIR analysis was conducted to identify functional groups in biomass, biochar, and the composite before and after adsorption, as shown in Figure 2. At 3444.33 cm^{-1}, the stretching vibration of hydroxyl groups becomes observable, with reduced transmittance due to water evaporation during pyrolysis [43]. The 2980.12 cm^{-1} peak shows aliphatic CH_2 groups that disappear during pyrolysis. CO_2 is identified at 2372.2 cm^{-1} [44], while the 1658.21 cm^{-1} peak corresponds to C=O vibrations in hemicellulose [45]. The 1526.76 cm^{-1} band indicates C=C stretching in aromatic rings [46], and 1050.28 cm^{-1} shows C−O in ester groups [44].

Distinct changes in the composite are evident before and after adsorption, aligning with Qureashi et al. (2023), where the C−H peak at 1463.72 cm^{-1} and Fe−O at 655.24 cm^{-1} confirm nZVI attachment to biochar. After Cr(VI) adsorption, there are minor shifts in the FTIR peaks, with the O–H absorption peak increasing from 3444.33 cm^{-1} to 3460.80 cm^{-1}. Additionally, the C–OH and O–H bond vibrations in phenolic and carboxyl groups decrease from 1126.242 cm^{-1} to 1122.385 cm^{-1}, suggesting the involvement of these groups in Cr(VI) adsorption by the biochar/nZVI composite.

3.3. SEM

The SEM analysis was conducted to examine the morphology of the SB biomass, biochar, and the composite before and after adsorption, as shown in Figure 3. In Figure 3(A), the SB biomass displays a fibrous structure with distinct channels and pores within its matrix. This porous morphology is critical as it offers a large surface area that can aid the adsorption process once the biomass is converted into biochar and integrated with nano zero-valent iron (nZVI). The surface of the raw biomass appears relatively smooth, reflecting the natural cellular structure characteristic of lignocellulosic materials. Following conversion to biochar, Figure 3(B) reveals a honeycomb-like pattern with well-defined pores and a rougher texture compared to the raw biomass. This structural transformation results from thermal decomposition during pyrolysis, which creates additional adsorption sites and increases the surface area. These features are vital for biochar's function as a support material for nZVI particles in the composite, as they enable effective particle loading and enhance the composite's contaminant adsorption capacity.

Figure 3(C) shows the composite before adsorption; nZVI particles were distributed evenly throughout the biochar matrix, with no visible signs of aggregation. The absence of particle clumping indicated systematic adsorption of nZVI on the surface and within the biochar pores, maximizing the composite's potential for heavy metal adsorption. This even distribution is crucial, as it promotes optimal contact between the nZVI and contaminants. A similar finding was observed by [47], who noted a uniform spread of nZVI particles without clustering in activated carbon-nZVI composites. After adsorption, as depicted in Figure 3(D), the composite's morphology changes significantly, with a notable reduction of nZVI particles observed. This change is attributed to the dissolution of nZVI particles under acidic conditions (pH 2). The dissolution process enables efficient interaction between Cr(VI) and the nZVI particles [46,47]. Biochar acts as a stabilizing matrix, embedding the nZVI particles and preventing agglomeration, which is typically caused by the magnetic forces between nZVI molecules. This stabilization maintains the reactivity of nZVI during the adsorption process. Additionally, biochar's functional groups, such as hydroxyl and carboxyl, facilitate adsorption through complexation and ion exchange mechanisms [48,49]. This synergy between biochar and nZVI highlights the composite's enhanced capacity for Cr(VI) removal.

3.4. BET

Table 2 presents the BET surface area analysis for biomass, biochar, and composites before and after adsorption. The biochar produced from SB using plasma pyrolysis exhibited a surface area of 87.50 m^2/g, a significant increase from the initial biomass surface area of 0.062 m^2/g. This highlights the effectiveness of plasma pyrolysis in enhancing biochar's surface area, as compared to oxidation or gasification methods, which yield 27.49 m^2/g [52].

According to [53], biochar surface areas typically range between 8 and 132 m^2/g, indicating that plasma pyrolysis results in biochar within a favorable range for adsorption applications. A larger surface area is advantageous as it provides more sites for contaminant adsorption.

The surface area varied when sugarcane bagasse biochar was composited with nZVI particles in different ratios. The surface area for the 1:1 composite before adsorption was 23.27 m^2/g, while for the 2:1 and 3:1 ratios, it is 34.56 m^2/g and 46.47 m^2/g, respectively. The decrease in surface area relative to pure biochar was attributed to the nZVI particles blocking the pores of the biochar, limiting available surface area [47]. Nonetheless, all composite ratios maintain significant surface areas suitable for adsorption.

After Cr(VI) adsorption, the surface areas of the composites changed to 28.72 m^2/g for the 1:1 ratio, 27.45 m^2/g for the 2:1 ratio, and 29.90 m^2/g for the 3:1 ratio. The reduction in surface area after Cr(VI) adsorption onto the SBB/nZVI composite adsorbent was primarily caused by the occupation of active adsorption sites on the composite surface [54]. During the adsorption process, negatively charged Cr(VI) ions interacted with positively charged sites on the composite adsorbent, particularly under acidic conditions (e.g., pH 2) where protonation occurred. This electrostatic interaction facilitated the binding of Cr(VI) ions to the surface, effectively blocking active sites and reducing the available surface area [54,55]. Additionally, the nZVI component in the composite reduced Cr(VI) to Cr(III), which could lead to the precipitation of Cr(III) onto the surface. This precipitation further occupied adsorption sites and altered the composite's porosity. As a result, the combination of site occupation, electrostatic interactions, and precipitation processes contributed to the observed reduction in surface area after Cr(VI) adsorption [54,55].

3.5. VSM

Based on Table 3 and Figure 4, the magnetic properties of the composite material before and after the adsorption process exhibited significant changes in parameters such as saturation magnetization (Ms), remanent magnetization (Mr), and coercivity (Hc). The saturation magnetization decreased from 0.1870 emu/g before adsorption to 0.001 emu/g afterward, indicating a substantial reduction in the composite's ability to be magnetized, likely due to the coverage of magnetic particles by the adsorbed substance or changes in their structure. Similarly, remanent magnetization dropped from 0.0848 emu/g to 0.0468 emu/g post-adsorption, reflecting a decreased retention of magnetization. The coercivity also increased significantly from 10 to 30,000 Oe, suggesting that the material requires a stronger external magnetic field to reduce its magnetization to zero after saturation.

The declining magnetization of nZVI was influenced as a result of the oxidation of nZVI. These observations align with the mechanisms of Cr(VI) removal, as the reduction process involves the oxidation of nZVI to various iron oxides (e.g., FeO, Fe_2O_3, Fe_3O_4), which are less magnetic. The decline in magnetic properties supports the consumption of nZVI during reduction and its transformation into non-magnetic phases. Furthermore, the oxidation process, influenced by exposure to oxygen in the air atmosphere adsorption environment, reduces magnetic susceptibility and alters the composite's structural and chemical characteristics, as discussed by [27]. This interaction leads to oxidation, forming various iron oxides such as FeO, Fe_2O_3, and Fe_3O_4. Oxidation alters the chemical state of iron and impacts its magnetic properties, reducing magnetization due to the formation of non-magnetic oxide phases that replace the zero-valent iron core [57]. The oxidation process decreases magnetic susceptibility as the oxide layers hinder magnetic interactions [58].

3.6. Zeta Potential

Figure 5 shows that the zeta potential value decreased as the pH of the solution increased. Under acidic conditions (pH 2), the zeta potential of SBB/nZVI composite adsorbent after adsorption reached –3.9 mV because the positively charged composite adsorbent (3.32 mV) successfully binds to the negatively charged Cr(VI) metal (-17.23 mV). However, in neutral and alkaline conditions, the potential zeta values decreased to -33.03 mV and -33.93 mV, respectively. This was due to the increase in OH^- ions that inhibited the binding of Cr(VI) so that the negative charge of the composite (pH 6 = -23.07 mV and pH 12 = -28.83 mV) and Cr(VI) (pH 6 = -37.16 mV and pH 12 = -48.83 mV) remained high and the adsorption efficiency decreases. This decrease in potential zeta indicated that H^+ ions increase the potential zeta value, while OH- ions contribute to its decrease. At low pH, Cr(VI) was more reactive and quickly reacted with protons, so the potential zeta was higher, while at high pH, Cr(VI) was less reactive, and the potential zeta decreased. This characteristic was in line with the results of a similar study that showed that biochar/nZVI had a higher potential zeta value at acidic pH and lower at alkaline pH, confirming that the composite surface was cationic, while Cr(VI) is anionic in nature [58,59].

3.7. Particle Size Distribution

The particle size distribution of the SBB/nZVI composite adsorbent was analyzed using zeta size measurements, with the results presented in Figure 6. The x-axis of Figure 6 illustrates the equivalent circle diameter, defined as the diameter of the particles under the assumption that they are spherical. It is crucial to recognize that the x-axis has a

logarithmic scale; thus, although the particle size distribution seems normal, it is right-skewed. The y-axis represents the signal strength for each particle diameter, offering a comparative assessment of the quantity of particles corresponding to each diameter. The mean particle size before treatment, as determined by the Zetasizer, was 415.8 ± 66.65 nm.

3.8. Effectiveness of Adsorbent on Cr(VI) *Adsorption*

3.8.1. Effect of initial concentration and contact time

The adsorption capacity of the composite adsorbents (SBB/nZVI) was significantly influenced by the concentration of the Cr(VI) solution and the contact time. Figure 7 illustrates the impact of contact time and initial solution concentration on the Cr(VI) adsorption capacity for biochar and composites with mass ratios of 1:1, 2:1, and 3:1. The findings indicate that as contact time increased, there was a notable enhancement in Cr(VI) adsorption capacity, particularly at the onset, due to the high concentration of Cr(VI) ions in the solution, which reduced mass transfer resistance between the adsorbent and the solution. Furthermore, higher initial concentrations generated a greater driving force that expedited the adsorption process. The peak adsorption capacity of 112.41 mg/g was achieved with the 3:1 SBB/nZVI composite at a Cr(VI) concentration of 175 ppm and a contact time of 180 minutes. However, at concentrations of 200 ppm, the adsorption capacity declined to 102.89 mg/g as the adsorbent pores became saturated with Cr(VI) ions, which limited further adsorption. The adsorption capacity between 175 ppm and 200 ppm declined by around 8.48%, which is why the adsorption process for other adsorbents stopped at 175 ppm (Figure 8(A)). As contact time increased, the interaction between Cr(VI) ions and the adsorbent enhanced, with the adsorption process being rapid during the first 60 minutes. After this period, the increase in adsorption became minimal, suggesting that the process was nearing equilibrium. This pattern was consistent across all adsorbent ratios, resulting in the saturation of the adsorbent surface and a reduction in adsorption capacity [61].

3.8.2. Effect of pH

The influence of solution pH on the Cr(VI) adsorption process was thoroughly examined, as pH plays a pivotal role in regulating Cr(VI) adsorption. Changes in pH can significantly impact the surface charge distribution between the adsorbent and the contaminant due to protonation and deprotonation reactions occurring in the adsorbent's functional groups. Identifying the optimal pH in this study was essential to quantify how acidity affects Cr(VI) adsorption efficiency. Figure 8(B) illustrates the effect of pH on Cr(VI) adsorption using the composite of SBB/nZVI.

The findings revealed lower pH levels promoted higher Cr(VI) adsorption. The most favorable adsorption capacity across all SBB/nZVI composites occurred at a pH of 2, and removal efficiency was 64.21%, 54.33%, 49.39%, and 44.45% on variations 3:1, 2:1, 1:1, and biochar, respectively. Maximum adsorption capacities reached 112.41 mg/g (3:1), 95.12 mg/g (2:1), 86.47 mg/g (1:1), and 77.82 mg/g for biochar alone.

This indicates that the optimum pH for Cr(VI) adsorption using the composite adsorbent is in acidic conditions, specifically at pH 2 [27]. On the other hand, the adsorbent surface contains abundant Fe–OH groups, which bond with H^+ from the medium, causing the particle surface to become positively charged and protonated. This leads to electrostatic interactions with chromium-containing anions in the aqueous solution [23]. As pH increases, the active sites on the surface of the SBB/nZVI composite undergo deprotonation, increasing the negative surface charge, which, combined with the higher OH^- concentration in the solution, results in repulsion and competitive adsorption with chromium-containing anions, thereby reducing the adsorption capacity [62]. This condition was linear with the zeta potential value, which resulted in the positively charged composite adsorbent (3.32 mV) binding to the negatively charged Cr(VI) metal (-17.23 mV) in an acidic condition (pH 2). Then, in neutral and alkaline conditions, the potential zeta values of the composite adsorbent decreased to -23.07 mV and -28.83 mV, respectively, so that the negative charge of the composite and Cr(VI) (pH 6 = -37.16 mV and pH 12 = -48.83 mV) resulted in repulsion causing the adsorption efficiency decreases.

Then, under acidic conditions (pH 2), the chemical reduction of Cr(VI) by nZVI was caused by the dissolution of nZVI particles. The dissolution process facilitated effective interaction between Cr(VI) and the nZVI particles [46,47]. Biochar serves as a stabilizing matrix that embeds nZVI particles, thereby preventing agglomeration typically induced by the magnetic forces among nZVI molecules. The stabilization preserves the reactivity of nZVI throughout the adsorption process. Biochar's functional groups, including hydroxyl and carboxyl, enhance adsorption via complexation and ion exchange mechanisms [48,49].

3.8.3. Effect of Adsorbent Dosage

Figure 8(C) illustrates that increased adsorbent dosage led to increased Cr(VI) removal efficiency. The porous structure of the adsorbent aided in Cr(VI) adsorption, allowing Cr(VI) ions to attach to its surface and form a thin film during the process. Although higher dosages provided a larger surface area and more active sites for adsorption, they reduced adsorbed Cr(VI), which aligned with the findings of [63]. At lower dosages, the surface became saturated

with Cr(VI), leading to higher adsorption; however, considerable amounts of Cr(VI) remained in the solution, consistent with the observations of [64]. The study demonstrated that the SBB/nZVI (3:1) composition consistently achieved the highest adsorption across different dosages. Removal efficiency were 64.21%, 54.33%, 49.39%, 44.45% on variations 3:1, 2:1, 1:1 and biochar, respectively. The maximum adsorption for the SBB/nZVI composites of 3:1, 2:1, 1:1, and biochar occurred at a dosage of 1 g/L, yielding corresponding values of 112.41 mg/g, 95.12 mg/g, 86.47 mg/g, and 77.82 mg/g, respectively.

3.9. Adsorption Isotherm

Figure 9 indicates that the Freundlich model was the most suitable adsorption isotherm model for the adsorption of Cr(VI) by the SBB/nZVI adsorbent. This conclusion is supported by the R^2 value of the Freundlich isotherm adsorption model for all adsorbent compositions, which was closer to 1 compared to the R^2 obtained from all models. The parameter values for both adsorption isotherms are detailed in Table 5 and Figure 9. The Freundlich isotherm model suggests that adsorption occurs in multiple layers on a heterogeneous surface.

3.10. Adsorption Kinetics

Figure 10 shows that the regression value for the pseudo-second-order kinetics model was higher than all kinetics models, which indicated that the adsorption kinetics model in this study followed the pseudo-second-order model. A process in the pseudo-second-order occurred when the adsorption rate was proportional to the square of the difference between the adsorption capacity in equilibrium and the adsorption capacity at a given time ($1/Ct - 1/Co = kt$). This model shows the presence of a chemical effect in the adsorption process, known as chemisorption, in which there was an interaction between the Cr(VI) metal (anionic) and the composite adsorbent surface (cationic) [65]. In addition, [66] stated that the pseudo-second-order kinetics model reflects the physicochemical interaction between the two phases, which can be seen from the increased adsorption efficiency and adsorbent dose. This phenomenon shows that the molecular attraction between the dissolved substance and the adsorbent surface is stronger than the interaction between the dissolved substance in the solution.

3.11. Adsorption Mechanism

The adsorption mechanism identified in this study incorporates chemisorption and physisorption, as this type of adsorption chemically binds ions while facilitating their easy release to promote ion exchange. This dual

449 mechanism is supported by the isotherm model analysis, which follows the Freundlich isotherm and the reaction
450 kinetics corresponding to a pseudo-second-order. Chemisorption is characterized by the chemical interactions
451 between the adsorbent and the adsorbate, involving electron transfer between the anionic Cr(VI) metal and the cationic
452 surface of the adsorbent. [67] state that the bonds formed during chemical adsorption are irreversible, involving solid
453 connections that are challenging to disrupt. FTIR analysis of the adsorbent post-adsorption, the impact of pH on the
454 Cr(VI) metal solution, BET test results, and adsorption isotherm analyses provide evidence of this chemical
455 adsorption.

456 Physisorption occurs through van der Waals forces between Cr(VI) ions and the porous surface of biochar,
457 which has a significantly enhanced surface area after plasma pyrolysis. This porous structure offers numerous sites
458 for the physical attachment of Cr(VI) ions [63,64]. In addition, chemical adsorption involved the formation of
459 chemical bonds between Cr(VI) and the adsorbent surface, a process further enhanced by nZVI [65,66]. The changes
460 in functional groups evidence this detected through FTIR characterization before and after adsorption, indicating
461 substantial chemical interactions.

462 The removal of Cr(VI) by the biochar/nZVI composite involves a combination of adsorption and chemical
463 reduction processes, both of which significantly influence the material's properties. Nano zero-valent iron (nZVI)
464 plays a critical role not only as an adsorbent but also as a reductant, chemically transforming Cr(VI) into the less toxic
465 Cr(III). This reduction occurs as nZVI donates electrons to Cr(VI), facilitated by acidic conditions where nZVI
466 dissolves and generates Fe^{2+} ions. The reaction can be represented as:

467 $$Cr(VI) + 3Fe(0) + 7H^{+} \rightarrow Cr(III) + 3Fe(II) + 4H_2O$$

468 The Fe(II) produced in this reaction can further reduce Cr(VI) or oxidize to Fe(III), forming iron hydroxides
469 that co-precipitate Cr(III). This chemical reduction mechanism complements adsorption, where functional groups on
470 the biochar, such as hydroxyl and carboxyl groups, interact with Cr(VI) through complexation and ion exchange,
471 bringing it into proximity to nZVI for reduction.

472 Moreover, chemical reduction occurs where nZVI reduces Cr(VI) to Cr(III), a more stable and less toxic form.
473 This reduction is also reflected in the diminished magnetic strength of the composite after adsorption, as shown by
474 the VSM results [66,67]. Co-adsorption encompasses the simultaneous interactions of biochar and nZVI, which work

synergistically to capture and adsorb Cr(VI); biochar provides a large surface area, while nZVI acts as a reducing agent [73].

3.12. Desorption and recycling study of composite adsorbent of SBB/nZVI

A leaching study was conducted to evaluate the reusability of the composite adsorbent of SBB/nZVI 3:1 composite after Cr(VI) adsorption. Hydrochloric acid (HCl) was employed as the leaching agent to desorb Cr(VI) and restore the composite's adsorption capacity. Specifically, a 1 M HCl solution was used for the process, with a leaching duration of 30 minutes at room temperature. The choice of 1 M HCl was based on its strong desorbing capability, which effectively breaks the bonds between Cr(VI) ions and the active sites of the composite. This concentration provides a balance between efficiency and material stability, as higher concentrations could lead to excessive corrosion or degradation, while lower concentrations might be insufficient for complete desorption. Additionally, 1M HCl is widely recognized in adsorption-desorption studies as a standard concentration that ensures both performance and preservation of material integrity. Conducting the leaching process at room temperature further minimizes the risk of thermal damage, maintaining the composite's structural integrity.

As shown in Figure S3, the study's results revealed that the composite adsorbent of SBB/nZVI 3:1 retained a significant portion of its adsorption capacity after repeated use. After five adsorption-desorption cycles, the composite maintained 68.3% of its initial capacity, demonstrating excellent reusability and stability. Using 1 M HCl proved to be an efficient method for regenerating the composite, as it achieved high desorption efficiency without any observable material loss or degradation. Furthermore, the use of HCl is cost-effective due to its low cost and wide availability, making it a practical choice for large-scale applications. Additionally, the leachate containing Cr(VI) can be treated using conventional wastewater, ensuring sustainable and environmentally friendly disposal.

Overall, the study highlights the effectiveness of 1 M HCl in regenerating the composite adsorbent of SBB/nZVI 3:1 for Cr(VI) adsorption. The composite’s ability to retain its adsorption performance over multiple cycles, combined with the cost-effectiveness and practicality of HCl as a leaching agent, confirms its potential for repeated use in Cr(VI) removal. This finding underscores the composite’s economic and environmental advantages in wastewater treatment applications.

3.13. Comparison of SBB/nZVI adsorbent with adsorbents from the previous study for Cr(VI) removal

Several studies have been conducted to optimize adsorbents for Cr(VI) removal, such as oxidized and unoxidized activated carbon, olive wastes, biochar, and nZVI. Table 6 summarizes the results of these studies compared to the SBB and SBB/nZVI composite used in this study. The SBB and SBB/nZVI composite demonstrated significantly higher adsorption capacities. The maximum capacity of the SBB/nZVI adsorbent was 1.73-3.87 times greater than other adsorbents, with an optimal pH of 2, making it highly effective for Cr(VI) removal. This current study confirms the superior performance of biochar/nZVI composites in treating wastewater containing heavy metals like Cr(VI).

4. Conclusions

In summary, the composite adsorbent made from sugarcane bagasse biochar and nano zero-valent iron (nZVI) was successfully synthesized, exhibiting composite surface area of 37.44 m^2/g (1:1), 49.26 m^2/g (2:1), and 62.37 m^2/g (3:1) and crucial functional groups such as C–OH and O–H bond vibrations in phenolic and carboxyl groups which were conducive to adsorption. The composite demonstrated substantial adsorption capacity, especially at optimal dosages and high initial Cr(VI) concentrations. The composites adsorbent had an adsorption capacity of 86.47 mg/g (1:1), 95.12 mg/g (2:1), and 112.41 mg/g (3:1). The adsorption behavior aligned closely with the Freundlich isotherm model. The findings indicate that this composite adsorbent may function as an efficient recycling solution to enhance the value of agricultural waste, reduce air pollution, and further Indonesia's objectives for a circular economy and net-zero carbon emissions.

Ethical Approval and Consent to Participate

Not applicable.

Consent to Publish

Not applicable.

Authors Contributions

Denny Dermawan: Conceptualization, method investigation, data investigation, writing, editing, supervision, review. **Aulia Diva Satriavi**: Conceptualization, writing, editing, method investigation, data investigation. **Dyah Isna Nurhidayati:** Data investigation. **Rahmad Firnandi:** Data investigation. **Novi Eka Mayangsari:** Method investigation, data investigation. **Tarikh Aziz Ramadhani:** writing, review. **Dika Rahayu Widiana:** writing, review.

Anda Iviana Juniani: writing, review. **Dwi Rasy Mujiyanti**: writing, supervision, review. **Ya-Fen Wang**: writing, supervision, review.

Funding

This study was financially supported by the Directorate General of Vocational Education, Ministry of Education, Culture, Research, and Technology of Indonesia (Contract number: 279/PKS/D.D4/PPK.01.APTV/VII/2024), the Waste Treatment Engineering Study Program and Laboratory, Shipbuilding Institute of Polytechnic Surabaya, Department of Environmental Engineering and Center for Environmental Risk Management, Chung Yuan Christian University.

Competing Interests

The authors declare that there are no known competing financial interests or personal relationships that could have influenced the work described in this paper.

Availability of data and materials

Not applicable.

References

[1] C. C. Alvarez, M. E. Bravo Gómez, and A. Hernández Zavala, "Hexavalent chromium: Regulation and health effects," *Journal of Trace Elements in Medicine and Biology*, vol. 65, p. 126729, May 2021, doi: 10.1016/j.jtemb.2021.126729.

[2] P. Sharma, S. P. Singh, S. K. Parakh, and Y. W. Tong, "Health hazards of hexavalent chromium (Cr (VI)) and its microbial reduction," *Bioengineered*, vol. 13, no. 3, pp. 4923–4938, Mar. 2022, doi: 10.1080/21655979.2022.2037273.

[3] J. P. Wise, J. L. Young, J. Cai, and L. Cai, "Current understanding of hexavalent chromium [Cr(VI)] neurotoxicity and new perspectives," *Environ Int*, vol. 158, p. 106877, Jan. 2022, doi: 10.1016/j.envint.2021.106877.

[4] J. Chen, J. Ma, Q. Fan, W. Zhang, and R. Guo, "A sustainable chrome-free tanning approach based on Zr-MOFs functionalized with different metals through post-synthetic modification," *Chemical Engineering Journal*, vol. 474, p. 145453, Oct. 2023, doi: 10.1016/j.cej.2023.145453.

[5] R. Zhu, C. Yang, K. Li, R. Yu, G. Liu, and B. Peng, "A smart high chrome exhaustion and chrome-less tanning system based on chromium (III)-loaded nanoparticles for cleaner leather processing," *J Clean Prod*, vol. 277, p. 123278, Dec. 2020, doi: 10.1016/j.jclepro.2020.123278.

[6] K. Adamiak and A. Sionkowska, "Current methods of collagen cross-linking: Review," *Int J Biol Macromol*, vol. 161, pp. 550–560, Oct. 2020, doi: 10.1016/j.ijbiomac.2020.06.075.

[7] J. Khatun, A. Mukherjee, and D. Dhak, "Emerging Contaminants of Tannery Sludge and Their Environmental Impact and Health Hazards," in *Environmental Engineering and Waste Management*, Cham: Springer Nature Switzerland, 2024, pp. 3–28. doi: 10.1007/978-3-031-58441-1_1.

[8] J. Ma, N. Yang, Y. Li, D. Gao, B. Lyu, and J. Zhang, "A cleaner approach to tanning process of cattle hide upper suede leather: chrome-less polycarboxylate/montmorillonite nanocomposites as tanning agent," *Environmental Science and Pollution Research*, vol. 28, no. 29, pp. 39014–39025, Aug. 2021, doi: 10.1007/s11356-021-13324-8.

[9] A. Wahyu Nugraha, O. Suparno, and N. S Indrasti, "Analisis Material, Energi Dan Toksisitas (Met) Pada Industri Penyamakan Kulit Untuk Identifikasi Strategi Produksi Bersih," *Jurnal Teknologi Industri Pertanian*, vol. 28, no. 1, pp. 48–60, Apr. 2018, doi: 10.24961/j.tek.ind.pert.2018.28.1.48.

[10] Y. Xue *et al.*, "A walnut shell biochar-nano zero-valent iron composite membrane for the degradation of carbamazepine via persulfate activation," *Science of the Total Environment*, vol. 899, Nov. 2023, doi: 10.1016/j.scitotenv.2023.165535.

[11] S. Wijitkosum, "Biochar derived from agricultural wastes and wood residues for sustainable agricultural and environmental applications," *International Soil and Water Conservation Research*, vol. 10, no. 2, pp. 335–341, Jun. 2022, doi: 10.1016/j.iswcr.2021.09.006.

[12] C. Krongtaew Sakdaronnarong, N. Onsrithong, R. Suwankrua, and W. Jonglertjunya, "Improving enzymatic saccharification of sugarcane bagasse by biological/physico-chemical pretreatment using Trametes versicolor and Bacillus sp.," *Bioresources*, vol. 7, no. 3, pp. 3935–3947, Jul. 2012, doi: 10.15376/biores.7.3.3935-3947.

[13] H. Dewajani, W. Zamrudy, Z. Irfin, D. Ningtyas, and N. Mujibur Ridlo, "Utilization of Indonesian sugarcane bagasse into bio asphalt through pyrolysis process using zeolite-based catalyst," *Mater Today Proc*, vol. 87, pp. 383–389, 2023, doi: 10.1016/j.matpr.2023.04.171.

[14] Hugot, *Handbook of Cane Sugar Engineering*. Elsevier, 2014. doi: 10.1016/C2013-0-12437-3.

[15] B. A. Ezeonuegbu *et al.*, "Agricultural waste of sugarcane bagasse as efficient adsorbent for lead and nickel removal from untreated wastewater: Biosorption, equilibrium isotherms, kinetics and desorption studies," *Biotechnology Reports*, vol. 30, Jun. 2021, doi: 10.1016/j.btre.2021.e00614.

[16] W. Somyanonthanakun, R. Ahmed, V. Krongtong, and S. Thongmee, "Studies on the adsorption of Pb(II) from aqueous solutions using sugarcane bagasse-based modified activated carbon with nitric acid: Kinetic, isotherm and desorption," *Chemical Physics Impact*, vol. 6, Jun. 2023, doi: 10.1016/j.chphi.2023.100181.

[17] O. Karnitz *et al.*, "Adsorption of heavy metal ion from aqueous single metal solution by chemically modified sugarcane bagasse," *Bioresour Technol*, vol. 98, no. 6, pp. 1291–1297, Apr. 2007, doi: 10.1016/j.biortech.2006.05.013.

[18] N. T. Berghuis, N. F. Novianti, and P. J. Ratri, "Isolation of Lignin from Sugarcane Bagasse as an Adsorbent for Chromium Ion," *Makara J Sci*, vol. 27, no. 3, pp. 217–226, Sep. 2023, doi: 10.7454/mss.v27i3.1446.

[19] D. Dermawan *et al.*, "The potential of transforming rice straw (Oryza sativa) and golden shower (Cassia fistula) seed waste into high-efficiency biochar by atmospheric pressure microwave plasma," *Ind Crops Prod*, vol. 185, no. May, p. 115122, Oct. 2022, doi: 10.1016/j.indcrop.2022.115122.

[20] H. Kang, S. Choi, J. H. Lee, K. T. Kim, Y. H. Song, and D. H. Lee, "Plasma jet assisted carbonization and activation of coffee ground waste," *Environ Int*, vol. 145, Dec. 2020, doi: 10.1016/j.envint.2020.106113.

[21] D. Dermawan, D.-W. Tsai, G. S. Yudoyono, S.-J. You, and Y.-K. Hsieh, "Taguchi method optimization of syngas production via pineapple waste pyrolysis using atmospheric pressure microwave plasma," *Renew Energy*, vol. 231, p. 120962, Sep. 2024, doi: 10.1016/j.renene.2024.120962.

[22] K. Li *et al.*, "Nano zero valent iron in the 21st century: A data-driven visualization and analysis of research topics and trends," *J Clean Prod*, vol. 415, Aug. 2023, doi: 10.1016/j.jclepro.2023.137812.

[23] X. Li, L. Zeng, N. Wen, and D. Deng, "Critical roles of sulfidation solvent in controlling surface properties and the dechlorination reactivity of S-nZVI," *J Hazard Mater*, vol. 417, Sep. 2021, doi: 10.1016/j.jhazmat.2021.126014.

[24] Y. Fang *et al.*, "From nZVI to SNCs: development of a better material for pollutant removal in water," Mar. 01, 2018, *Springer Verlag*. doi: 10.1007/s11356-017-1143-3.

[25] H. Xu *et al.*, "A novel preparation of S-nZVI and its high efficient removal of Cr(VI) in aqueous solution," *J Hazard Mater*, vol. 416, Aug. 2021, doi: 10.1016/j.jhazmat.2021.125924.

[26] T. Phenrat, N. Saleh, K. Sirk, R. D. Tilton, and G. V. Lowry, "Aggregation and sedimentation of aqueous nanoscale zerovalent iron dispersions," *Environ Sci Technol*, vol. 41, no. 1, pp. 284–290, Jan. 2007, doi: 10.1021/es061349a.

[27] A. Shan *et al.*, "Synthesis of nZVI-Ni@BC composite as a stable catalyst to activate persulfate: Trichloroethylene degradation and insight mechanism," *J Environ Chem Eng*, vol. 9, no. 1, Feb. 2021, doi: 10.1016/j.jece.2020.104808.

[28] A. Baldermann, S. Kaufhold, R. Dohrmann, C. Baldermann, I. Letofsky-Papst, and M. Dietzel, "A novel nZVI–bentonite nanocomposite to remove trichloroethene (TCE) from solution," *Chemosphere*, vol. 282, Nov. 2021, doi: 10.1016/j.chemosphere.2021.131018.

[29] E. Petala *et al.*, "Nanoscale zero-valent iron supported on mesoporous silica: Characterization and reactivity for Cr(VI) removal from aqueous solution," *J Hazard Mater*, vol. 261, pp. 295–306, Oct. 2013, doi: 10.1016/j.jhazmat.2013.07.046.

[30] Z. Chen, T. Wang, X. Jin, Z. Chen, M. Megharaj, and R. Naidu, "Multifunctional kaolinite-supported nanoscale zero-valent iron used for the adsorption and degradation of crystal violet in aqueous solution," *J Colloid Interface Sci*, vol. 398, pp. 59–66, May 2013, doi: 10.1016/j.jcis.2013.02.020.

[31] R. Fu, Y. Yang, Z. Xu, X. Zhang, X. Guo, and D. Bi, "The removal of chromium (VI) and lead (II) from groundwater using sepiolite-supported nanoscale zero-valent iron (S-NZVI)," *Chemosphere*, vol. 138, pp. 726–734, Nov. 2015, doi: 10.1016/j.chemosphere.2015.07.051.

[32] S. Mortazavian, H. An, D. Chun, and J. Moon, "Activated carbon impregnated by zero-valent iron nanoparticles (AC/nZVI) optimized for simultaneous adsorption and reduction of aqueous hexavalent chromium: Material characterizations and kinetic studies," *Chemical Engineering Journal*, vol. 353, pp. 781–795, Dec. 2018, doi: 10.1016/j.cej.2018.07.170.

[33] S. Wang *et al.*, "Biochar-supported nZVI (nZVI/BC) for contaminant removal from soil and water: A critical review," *J Hazard Mater*, vol. 373, pp. 820–834, Jul. 2019, doi: 10.1016/j.jhazmat.2019.03.080.

[34] M. Ahmadi, E. Kouhgardi, and B. Ramavandi, "Physico-chemical study of dew melon peel biochar for chromium attenuation from simulated and actual wastewaters," *Korean Journal of Chemical Engineering*, vol. 33, no. 9, pp. 2589–2601, Sep. 2016, doi: 10.1007/s11814-016-0135-1.

[35] I. Ullah, R. Nadeem, M. Iqbal, and Q. Manzoor, "Biosorption of chromium onto native and immobilized sugarcane bagasse waste biomass," *Ecol Eng*, vol. 60, pp. 99–107, Nov. 2013, doi: 10.1016/j.ecoleng.2013.07.028.

[36] M. A. Selimin, A. F. A. Latif, C. W. Lee, M. S. Muhamad, H. Basri, and T. C. Lee, "Adsorption efficiency of hydroxyapatite synthesised from black tilapia fish scales for chromium (VI) removal," *Mater Today Proc*, vol. 57, pp. 1142–1146, 2022.

[37] I. H. Ifijen *et al.*, "The removal of nickel and lead ions from aqueous solutions using green synthesized silica microparticles," *Heliyon*, vol. 6, no. 9, 2020, doi: 10.1016/j.heliyon.2020.e04907.

[38] D. Dermawan *et al.*, "The potential of transforming rice straw (Oryza sativa) and golden shower (Cassia fistula) seed waste into high-efficiency biochar by atmospheric pressure microwave plasma," *Ind Crops Prod*, vol. 185, no. May, p. 115122, Oct. 2022, doi: 10.1016/j.indcrop.2022.115122.

[39] S. Yoo, S. S. Kelley, D. C. Tilotta, and S. Park, "Structural Characterization of Loblolly Pine Derived Biochar by X-ray Diffraction and Electron Energy Loss Spectroscopy," *ACS Sustain Chem Eng*, vol. 6, no. 2, pp. 2621–2629, Feb. 2018, doi: 10.1021/acssuschemeng.7b04119.

[40] S. Martins Torres, V. Estolano de Lima, P. de Azevedo Basto, N. T. de Araújo Júnior, and A. A. de Melo Neto, "Assessing the pozzolanic activity of sugarcane bagasse ash using X-ray diffraction," *Constr Build Mater*, vol. 264, Dec. 2020, doi: 10.1016/j.conbuildmat.2020.120684.

[41] M. Kurniati, D. Nurhayati, and A. Maddu, "Study of Structural and Electrical Conductivity of Sugarcane Bagasse-Carbon with Hydrothermal Carbonization," in *IOP Conference Series: Earth and Environmental Science*, Institute of Physics Publishing, Apr. 2017. doi: 10.1088/1755-1315/58/1/012049.

[42] M.-H. Jang, M. Lim, and Y. S. Hwang, "Potential environmental implications of nanoscale zero-valent iron particles for environmental remediation," *Environ Health Toxicol*, vol. 29, p. e2014022, Dec. 2014, doi: 10.5620/eht.e2014022.

[43] B. Chen, D. Zhou, and L. Zhu, "Transitional adsorption and partition of nonpolar and polar aromatic contaminants by biochars of pine needles with different pyrolytic temperatures," *Environ Sci Technol*, vol. 42, no. 14, pp. 5137–5143, Jul. 2008, doi: 10.1021/es8002684.

[44] J. A. Schott, C. L. Do-Thanh, W. Shan, N. G. Puskar, S. Dai, and S. M. Mahurin, "FTIR investigation of the interfacial properties and mechanisms of CO2 sorption in porous ionic liquids," *Green Chemical Engineering*, vol. 2, no. 4, pp. 392–401, Dec. 2021, doi: 10.1016/j.gce.2021.09.003.

[45] G. I. B. De Muñiz, M. E. Carneiro, S. Nisgoski, M. G. L. Ramirez, and W. L. E. Magalhães, "SEM and NIR characterization of four forest species charcoal," *Wood Sci Technol*, vol. 47, no. 4, pp. 815–823, Jul. 2013, doi: 10.1007/s00226-013-0539-6.

[46] A. S. Yargiç, R. Z. Yarbay Şahin, N. Özbay, and E. Önal, "Assessment of toxic copper(II) biosorption from aqueous solution by chemically-treated tomato waste," *J Clean Prod*, vol. 88, pp. 152–159, Feb. 2015, doi: 10.1016/j.jclepro.2014.05.087.

[47] S. Chen, M. Li, Y. Wu, and Y. Wang, "Activated carbon fiber-supported nano zero-valent iron on Cr(VI) removal," in *IOP Conference Series: Earth and Environmental Science*, IOP Publishing Ltd, Mar. 2021. doi: 10.1088/1755-1315/675/1/012170.

[48] C. Duan, J. Ren, L. Tao, H. Ren, M. Wang, and B. Wang, "Study of the Remediation Effect and Mechanism of Biochar-Loaded nZVI on Heavy Metal Contaminated Soil," *Sustainability (Switzerland)*, vol. 15, no. 24, Dec. 2023, doi: 10.3390/su152416753.

[49] S. Wei *et al.*, "Removal mechanism of Pb(ii) from soil by biochar-supported nanoscale zero-valent iron composite materials," *RSC Adv*, vol. 14, no. 26, pp. 18148–18160, Jun. 2024, doi: 10.1039/d4ra03357d.

[50] X. Wang *et al.*, "Study on Adsorption Characteristics of Heavy Metal Cd^{2+} by Biochar Obtained from Water Hyacinth," *Pol J Environ Stud*, vol. 31, no. 3, pp. 2301–2316, 2022, doi: 10.15244/pjoes/141045.

[51] B. Ibrahim Dan-Iya and M. Yunus Shukor, "Modelling the Effect of Nanoscale Zero-Valent Iron (nZVI), Biochar (BC) and Nanoscale Zero-Valent Iron/Biochar (nZVI/BC) on the Adsorption/Reduction of Nitrobenzene (NB)," 2020. [Online]. Available: https://journal.hibiscuspublisher.com/index.php/JEBAT

[52] K. O. Iwuozor, E. Chizitere Emenike, J. O. Ighalo, F. O. Omoarukhe, P. E. Omuku, and A. George Adeniyi, "A Review on the thermochemical conversion of sugarcane bagasse into biochar," Dec. 01, 2022, *Elsevier Ltd*. doi: 10.1016/j.clema.2022.100162.

[53] L. Leng *et al.*, "An overview on engineering the surface area and porosity of biochar," Apr. 01, 2021, *Elsevier B.V.* doi: 10.1016/j.scitotenv.2020.144204.

[54] X. L. Chen, F. Li, X. J. Xie, Z. Li, and L. Chen, "Nanoscale zero-valent iron and chitosan functionalized eichhornia crassipes biochar for efficient hexavalent chromium removal," *Int J Environ Res Public Health*, vol. 16, no. 17, Sep. 2019, doi: 10.3390/ijerph16173046.

[55] S. Xiang, Q. Zhou, M. Jin, L. Fu, and W. Wu, "Preparation of biochar-supported nanoscale zero-valent iron (nZVI@ BC) and its adsorption and degradation of chlortetracycline in water and soil," *Revista Materia*, vol. 29, no. 3, 2024, doi: 10.1590/1517-7076-RMAT-2024-0425.

[56] M. Yang, X. Zhang, and Y. Sun, "Remediation of Cr(VI) Polluted Groundwater Using Zero-Valent Iron Composites: Preparation, Modification, Mechanisms, and Environmental Implications," *Molecules*, vol. 29, no. 23, p. 5697, Dec. 2024, doi: 10.3390/molecules29235697.

[57] P. Boonruam, S. Soisuwan, P. Wattanachai, H. Morillas, and S. Upasen, "SOLVENT EFFECT ON ZERO-VALENT IRON NANOPARTICLES (nZVI) PREPARATION AND ITS THERMAL OXIDATION CHARACTERISTIC," 2020.

[58] A. Ansari *et al.*, "Synthesis of atmospherically stable zero-valent iron nanoparticles (Nzvi) for the efficient catalytic treatment of high-strength domestic wastewater," *Catalysts*, vol. 12, no. 1, Jan. 2022, doi: 10.3390/catal12010026.

[59] K. Liu *et al.*, "A highly porous animal bone-derived char with a superiority of promoting nZVI for Cr(VI) sequestration in agricultural soils," *Journal of Environmental Sciences*, vol. 104, pp. 27–39, Jun. 2021, doi: 10.1016/j.jes.2020.11.031.

[60] Z. Fan, Q. Zhang, B. Gao, M. Li, C. Liu, and Y. Qiu, "Removal of hexavalent chromium by biochar supported nZVI composite: Batch and fixed-bed column evaluations, mechanisms, and secondary contamination prevention," *Chemosphere*, vol. 217, pp. 85–94, Feb. 2019, doi: 10.1016/j.chemosphere.2018.11.009.

[61] Rusnam, A. T. Puari, N. R. Yanti, and Efrizal, "Utilisation of Exhausted Coffee Husk as Low-Cost Bio-Sorbent for Adsorption of Pb2+," *Trop Life Sci Res*, vol. 33, no. 3, pp. 229–252, 2022, doi: 10.21315/tlsr2022.33.3.12.

[62] Y. di Chen, S. H. Ho, D. Wang, Z. su Wei, J. S. Chang, and N. qi Ren, "Lead removal by a magnetic biochar derived from persulfate-ZVI treated sludge together with one-pot pyrolysis," *Bioresour Technol*, vol. 247, pp. 463–470, 2018, doi: 10.1016/j.biortech.2017.09.125.

[63] P. Bober *et al.*, "Polypyrrole Aerogels: Efficient Adsorbents of Cr(VI) Ions from Aqueous Solutions," *Gels*, vol. 9, no. 7, Jul. 2023, doi: 10.3390/gels9070582.

[64] S. Fang *et al.*, "Removal of Chromium (VI) by a Magnetic Nanoscale Zerovalent Iron–Assisted Chicken Manure-Derived Biochar: Adsorption Behavior and Synergetic Mechanism," *Front Bioeng Biotechnol*, vol. 10, Jul. 2022, doi: 10.3389/fbioe.2022.935525.

[65] X. Han, H. Zhang, C. Zhang, Y. Zhao, N. Zhang, and J. Liang, "Preparation of Sepiolite Nanofibers Supported Zero Valent Iron Composite Material for Catalytic Removal of Tetracycline in Aqueous Solution," *Front Chem*, vol. 9, Sep. 2021, doi: 10.3389/fchem.2021.736285.

[66] J. Bullen, S. Saleesongsom, K. Gallagher, and D. Weiss, "A Revised Pseudo-Second-Order Kinetic Model for Adsorption, Sensitive to Changes in Adsorbate and Adsorbent Concentrations," *Langmuir*, vol. 37, no. 10, p. pp, 2021, doi: 10.1021/acs.langmuir.1c00142i.

[67] O. D. Agboola and N. U. Benson, "Physisorption and Chemisorption Mechanisms Influencing Micro (Nano) Plastics-Organic Chemical Contaminants Interactions: A Review," May 28, 2021, *Frontiers Media S.A.* doi: 10.3389/fenvs.2021.678574.

[68] M. Mobarak *et al.*, "Insights into the adsorption performance and mechanism of Cr(VI) onto porous nanocomposite prepared from gossans and modified coal interface: Steric, energetic, and thermodynamic parameters interpretations," *Chin J Chem Eng*, vol. 61, pp. 118–128, Sep. 2023, doi: 10.1016/j.cjche.2023.02.016.

[69] S. A. L. Bachmann, I. V. J. Dávila, T. Calvete, and L. A. Féris, "Adsorption of Cr (VI) on lignocellulosic wastes adsorbents: an overview and further perspective," *International Journal of Environmental Science and Technology*, vol. 19, no. 12, pp. 12727–12748, Dec. 2022, doi: 10.1007/s13762-022-03928-z.

[70] B. Ren *et al.*, "Tracking the Molecular-Scale Mechanistic Pathway of Trapping-Bonding CTAB/Fe3O4-AS for High-Performance Cr(VI) Adsorption," *Chemical Engineering Journal*, vol. 497, p. 155053, Oct. 2024, doi: 10.1016/j.cej.2024.155053.

[71] X. Zhang, W. Wang, P. Tan, N. Meng, X. Cao, and Y. Zhang, "Study on the kinetics and mechanisms of Cr(VI) removal by nZVI modified with four modifiers," *Sep Purif Technol*, vol. 342, p. 127022, Aug. 2024, doi: 10.1016/j.seppur.2024.127022.

[72] E. Salama *et al.*, "The superior performance of silica gel supported nano zero-valent iron for simultaneous removal of Cr (VI)," *Sci Rep*, vol. 12, no. 1, p. 22443, Dec. 2022, doi: 10.1038/s41598-022-26612-1.

[73] H. A. El-Gawad, G. Kadry, H. A. Zahran, and M. H. Hussein, "Chromium Disarmament from Veritable Tanneries Sewer Water Utilizing Carbonic Rice Straw as a Sorbent: Optimization and Carbonic Rice Straw Characteristics," *Water Air Soil Pollut*, vol. 234, no. 10, Oct. 2023, doi: 10.1007/s11270-023-06644-7.

Table 1 XRD of biomass and biochar of SBB

Sample	2Θ (Main Reflections)	Crystallinity Index (%)	Crystal size (nm)
Biomass	35.3	15.58%	16.66
Biochar	35.1	14.81%	16.67

Table 2 BET surface area of biomass, biochar, biochar before and after adsorption, composite adsorbent before and after adsorption

Adsorbent Sample	Specific Surface Area (m^2/g)	Pore size (nm)	Pore volume (cm^3/g)
Biomass	0.062	131.2 nm	0.002 cm^3/g
Biochar	87.55	2.938 nm	0.064 cm^3/g
Biochar After Adsorption	43.59	1.074 nm	0.0023 cm^3/g
Composite Before Adsorption 1:1	23.27	14.56 nm	0.169 cm^3/g
Composite Before Adsorption 2:1	34.56	16.43 nm	0.095 cm^3/g
Composite Before Adsorption 3:1	46.47	38.08 nm	0.163 cm^3/g
Composite After Adsorption 1:1	28.72	7.041 nm	0.0483 cm^3/g
Composite After Adsorption 2:1	27.45	7.887 nm	0.056 cm^3/g
Composite After Adsorption 3:1	29.90	10.32 nm	0.077 cm^3/g

Table 3 VSM

Sample	Ms (emu/g)	Mr (emu/g)	Hc (Oe)
Composite Before Adsorption 3:1	0.1870	0.0848	30.000
Composite After Adsorption 3:1	0. 001	0.0468	1

Table 4 Fitting parameters of adsorption isotherm

Adsorption isotherm models	Parameters	Adsorbent composition (SBB/nZVI)			
		Biochar	1:1	2:1	3:1
Langmuir	Q_m (mg/g)	1.717	1.87	2.065	2.44
	K_L (L/mg)	-3166.351	-2622.778	-3330.789	-1493.860
	R^2	0.72643	0.72908	0.3314	0.73426
Freundlich	K_f (L/mg)	2.887	1.89	1.564	5.466
	1/n	0.3375	0.511	0.620	0.478
	R^2	0.99993	0.9999	0.99921	0.99969
Temkin	Bt (J/mol)	76.325	76.835	76.868	79.215
	At (L/mg)	0.077	0.084	0.092	0.109
	R^2	0.93178	0.9326	0.9398	0.93621
Dubinin-Radushkevich	B (mol^2/J^2)	2 x 10-8	1 x 10^{-7}	2 x 10^{-8}	1 x 10-7
	Qm (mg/g)	122.368	122.888	123.464	125.319
	R^2	0.81899	0.82199	0.8265	0.83525

Table 5 Kinetics order of adsorption

Adsorption kinetics order	Parameters	Adsorbent composition (SBB/nZVI)			
		Biochar	1:1	2:1	3:1
Pseudo 1st	Qe (mg/g)	80.59446704	80.07950871	95.37724233	103.0310089
	K (min^{-1})	-0.0003	-0.0004	-0.0003	-0.0004
	R^2	0.97658	0.99774	0.98787	0.99778
Pseudo 2nd	Qe (mg/g)	108.8139282	101.1122346	122.2493888	124.3781095
	K (g/mg min)	0.0002	0.0004	0.0002	0.0003
	R^2	0.98955	0.9998	0.9968	0.99977
Intraparticle Diffusion	B (mg/g)	166.29262	137.3440	154.65614	125.0295
	K (mg/g $min^{0.5}$)	-5.744	-4.103	-6.154	-5.128
	R^2	0.91765	0.91765	0.91765	0.91764
Elovich	B (mg/g min)	227.81316	220.5709	181.28723	179.9585
	A (g/mg)	-26.305	-28.184	-18.789	-23.487
	R^2	0.97466	0.97465	0.97466	0.97465

Table 6 Comparison with the previous research

Type of adsorbents	Carbonization process	Activation process	Optimum pH	Dosage (g/L)	Cr (VI) concentration (mg/L)	Adsorption Capacity (mg/g)	Specific surface area (m^2/g)	References
Dew melon peel biochar	Pyrolysis	-	6	1	100	98.6	196	(Ahmadi et al., 2016)
Rice straw-activated carbon	Using the oven at a temperature of 450 ± 20°C for 2 h	Using H_3PO_4 solution for 3 h at 100–130°C and stirred on an electrical stirrer at 240 rpm	3	5	30	29.34	-	El-Gawad et al., (2023)
Sugarcane bagasse biochar			3	0.1	100	80.6	-	(Ullah et al., 2013)
nZVI			4	0.5	45	27.8	-	Gao et al., (2022)
Activated carbon-nZVI			3	1	100	98.9	1087	Chen et al. (2021)
Sugarcana bagasse-magnetic			2	0.004	300	29.08	81.94	Liang et al., (2020)
Sugarcane bagasse biochar			2	1	175	77.84	87.50	**This Study**
Sugarcane bagasse biochar-nZVI			2	1	175	112.41	46.47	**This Study**

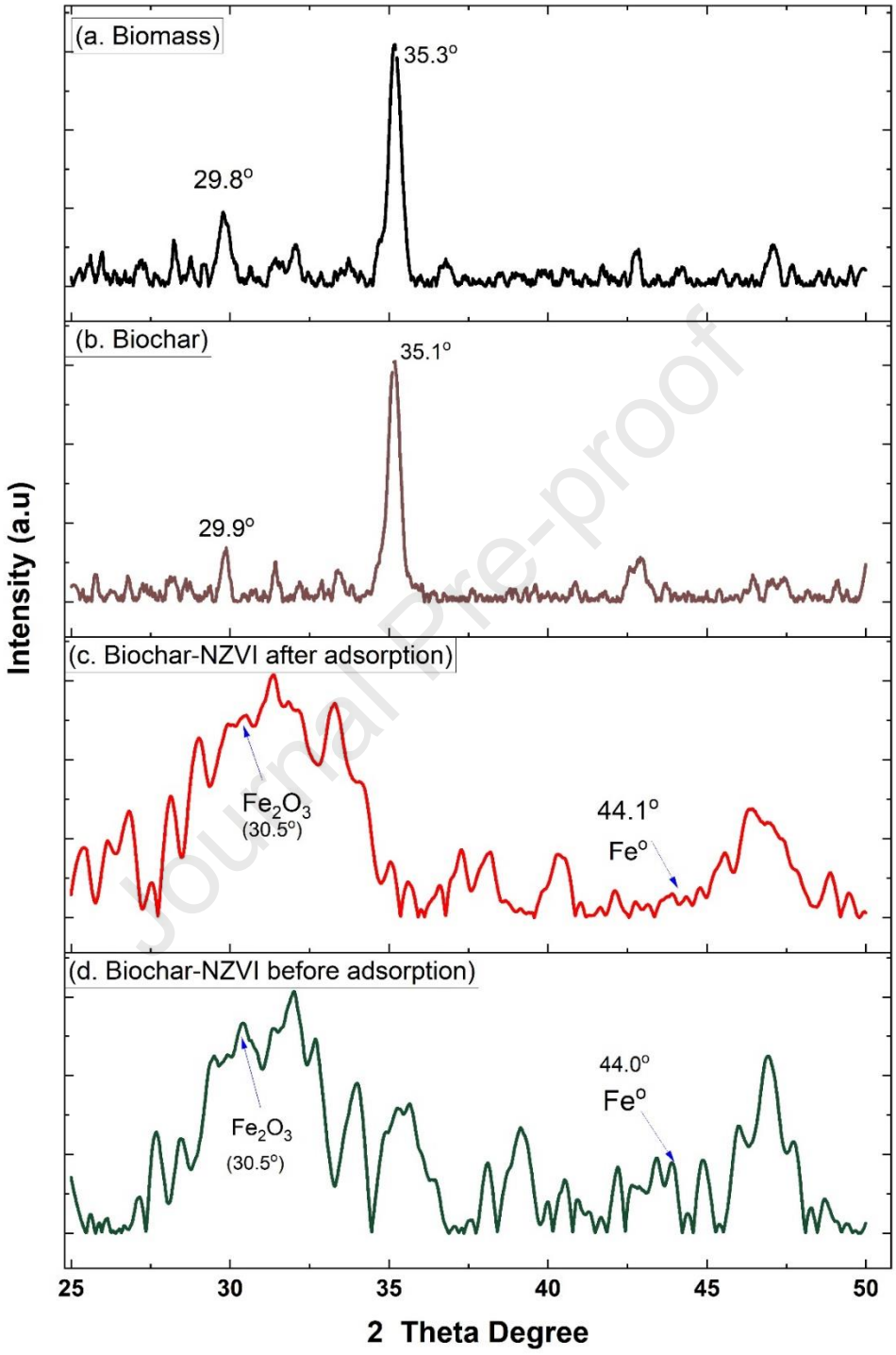

Figure 1 XRD Difractogram Pattern on SB Biomass, SB Biochar (SBB), composite adsorbent SBB/nZVI before adsorption, and composite adsorbent SBB/nZVI after adsorption

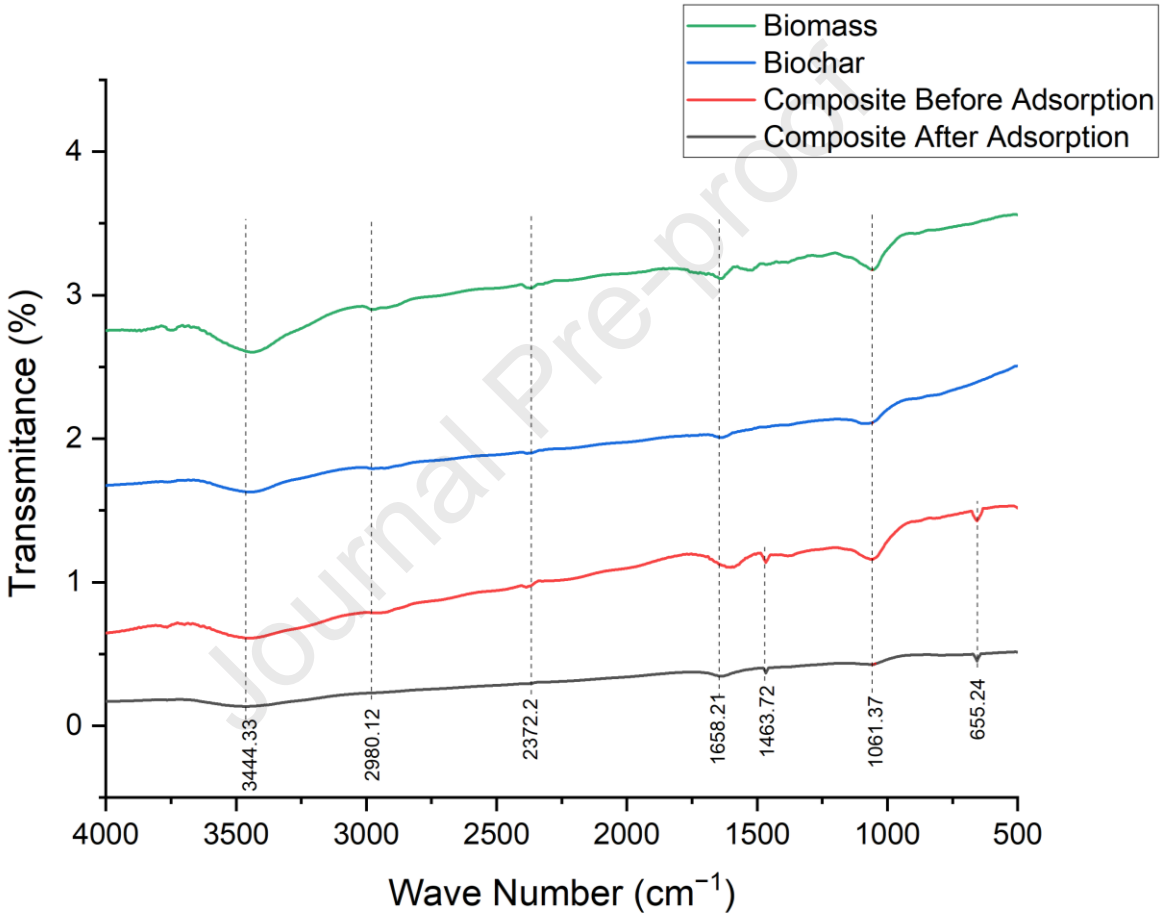

Figure 2 Comparison of Sugarcane Bagasse FTIR Spectrum, Bagasse Biochar, Composite Before Adsorption and Composite After Adsorption

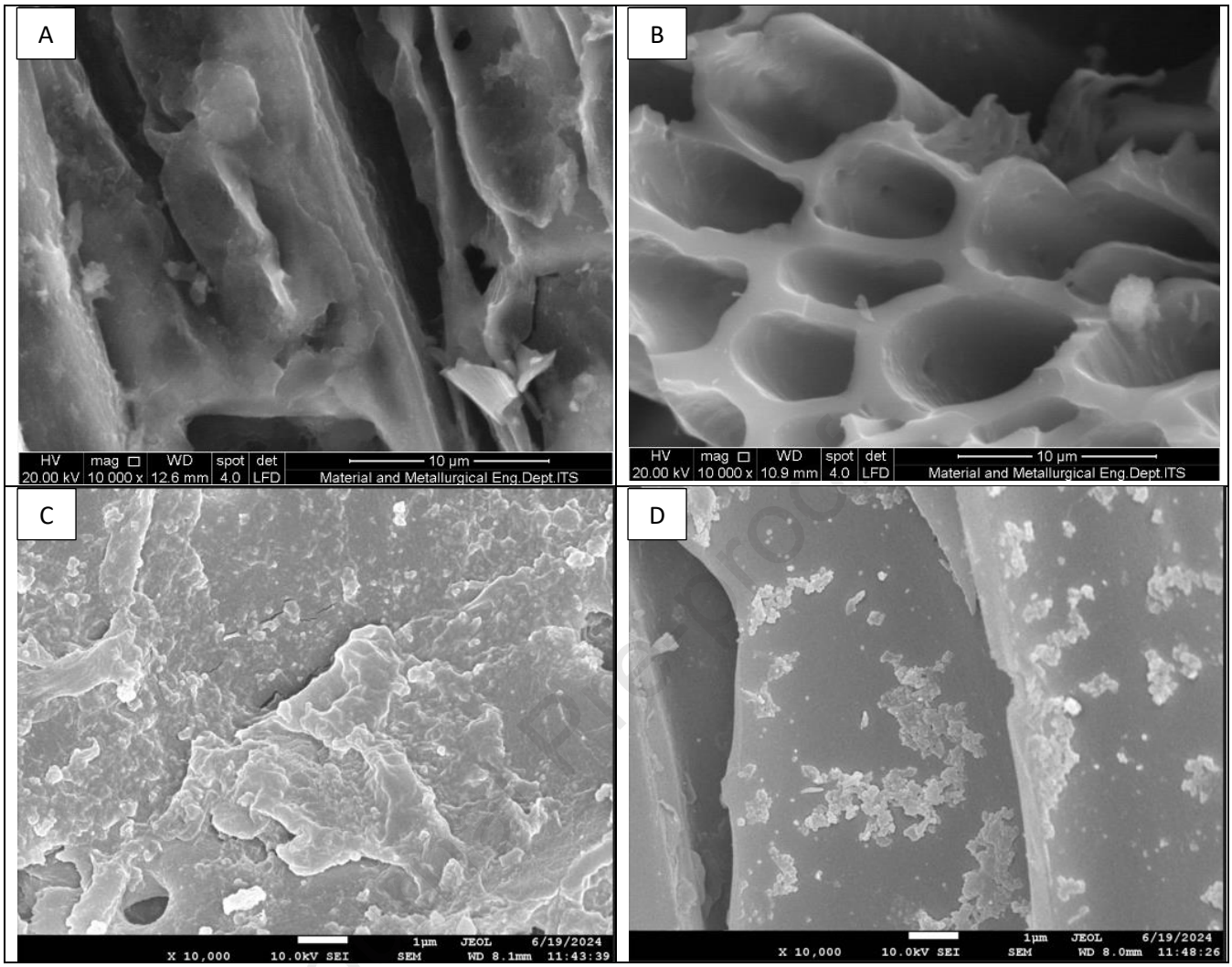

Figure 3 SEM Test Results of Sugarcane Bagasse Biomass (A), Biochar (B), Composite Before Adsorption (C), and Composite After Adsorption (D)

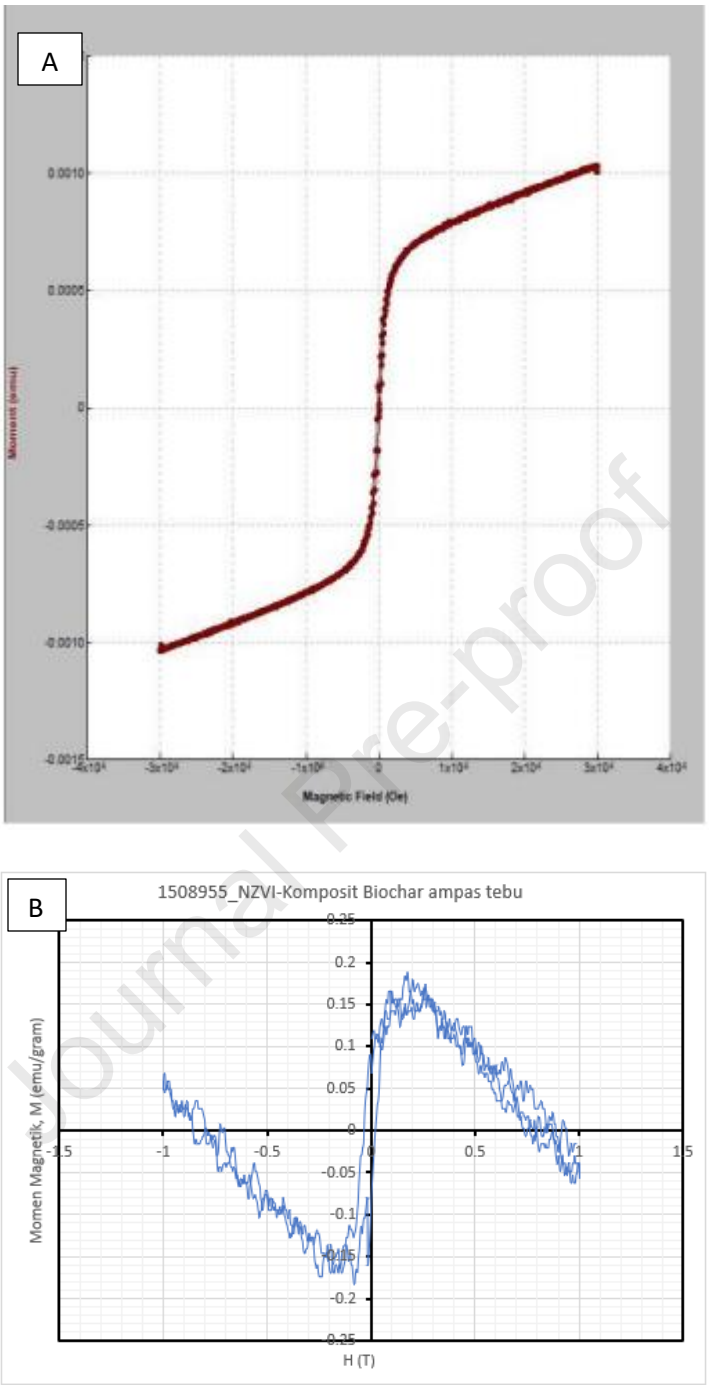

Figure 4 VSM Test Results of SBB/nZVI Composite with (a) Before Adsorption and (b) After Adsorption

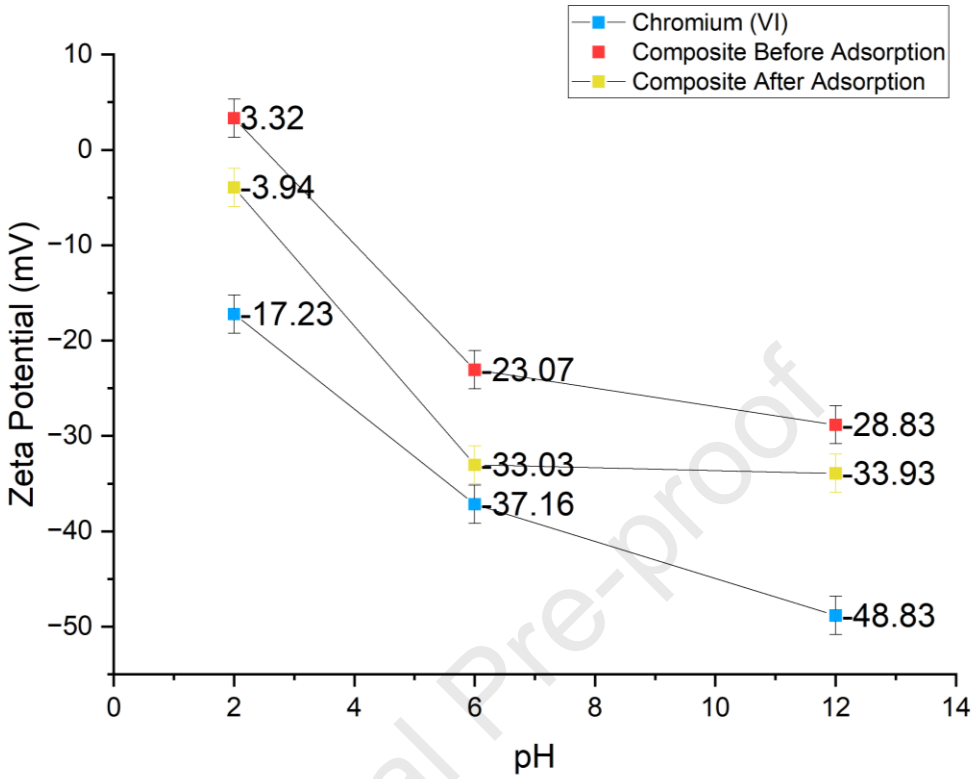

Figure 5 Zeta Potential on Cr(VI), composite adsorbent SBB/nZVI before adsorption, and composite adsorbent SBB/nZVI after adsorption

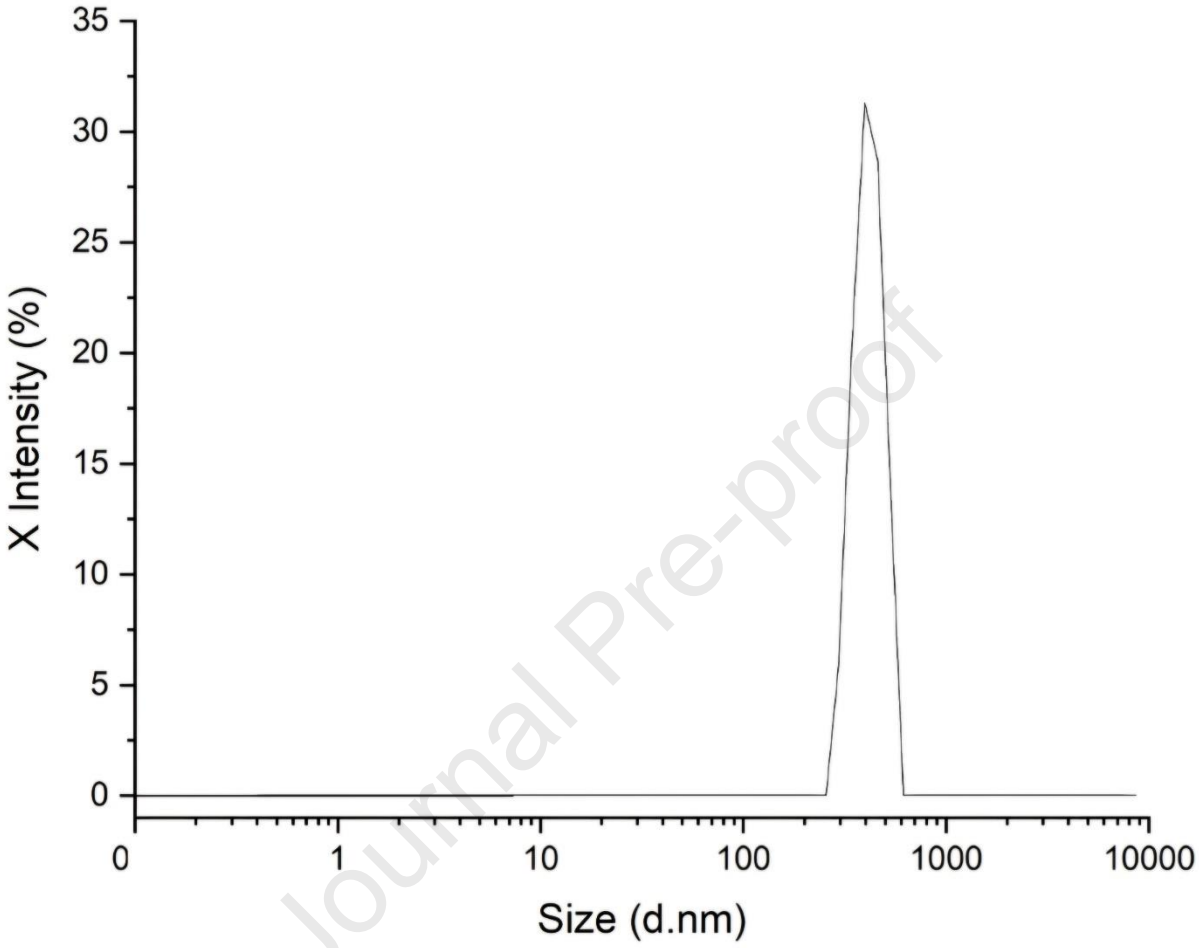

Figure 6 Particle size distribution of SBB/nZVI Composite Adsorbent

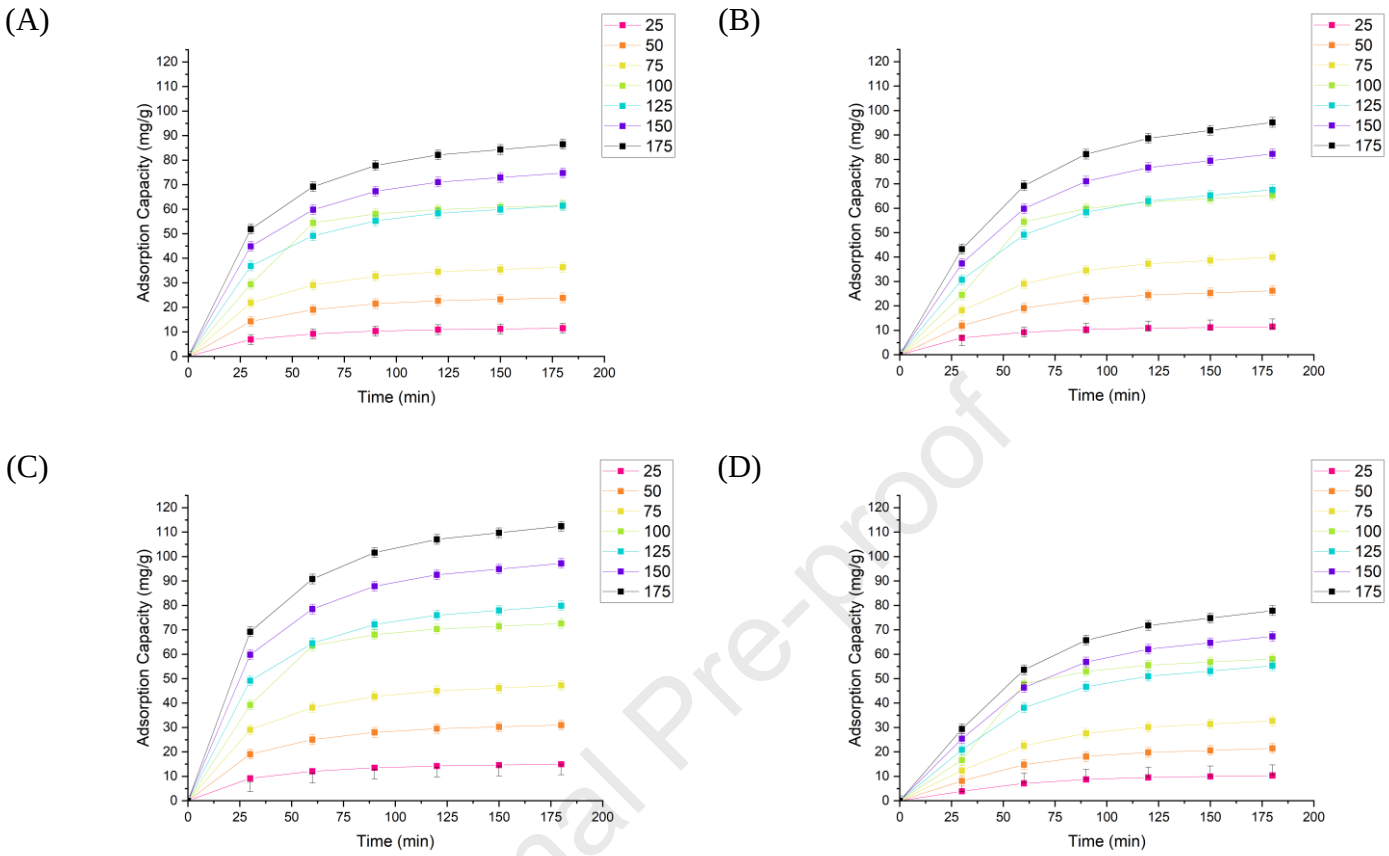

Figure 7 Effect of contact time and initial concentration of Cr(VI) adsorption

(A) 1:1, (B) 2:1, (C) 3:1, and (D) Biochar

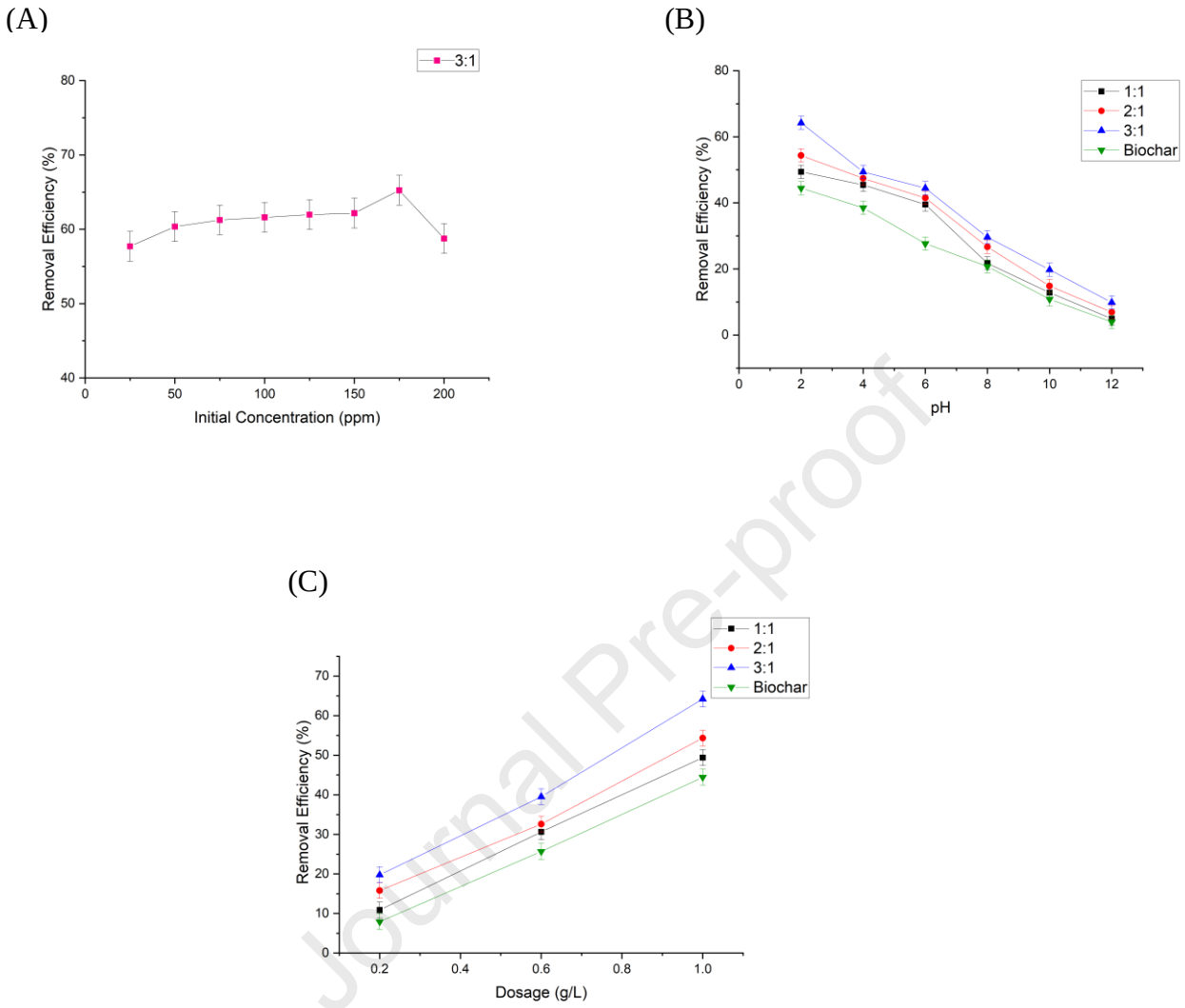

Figure 8 Adsorption capabilities of various materials: (a) SB biochar and composites of SBB/nZVI at ratios of (b) 1:1, (c) 2:1, and (d) 3:1. The performance is presented as a function of (A) Initial Cr(VI) concentration, (B) Initial pH solution, and (C) Adsorbent dosage

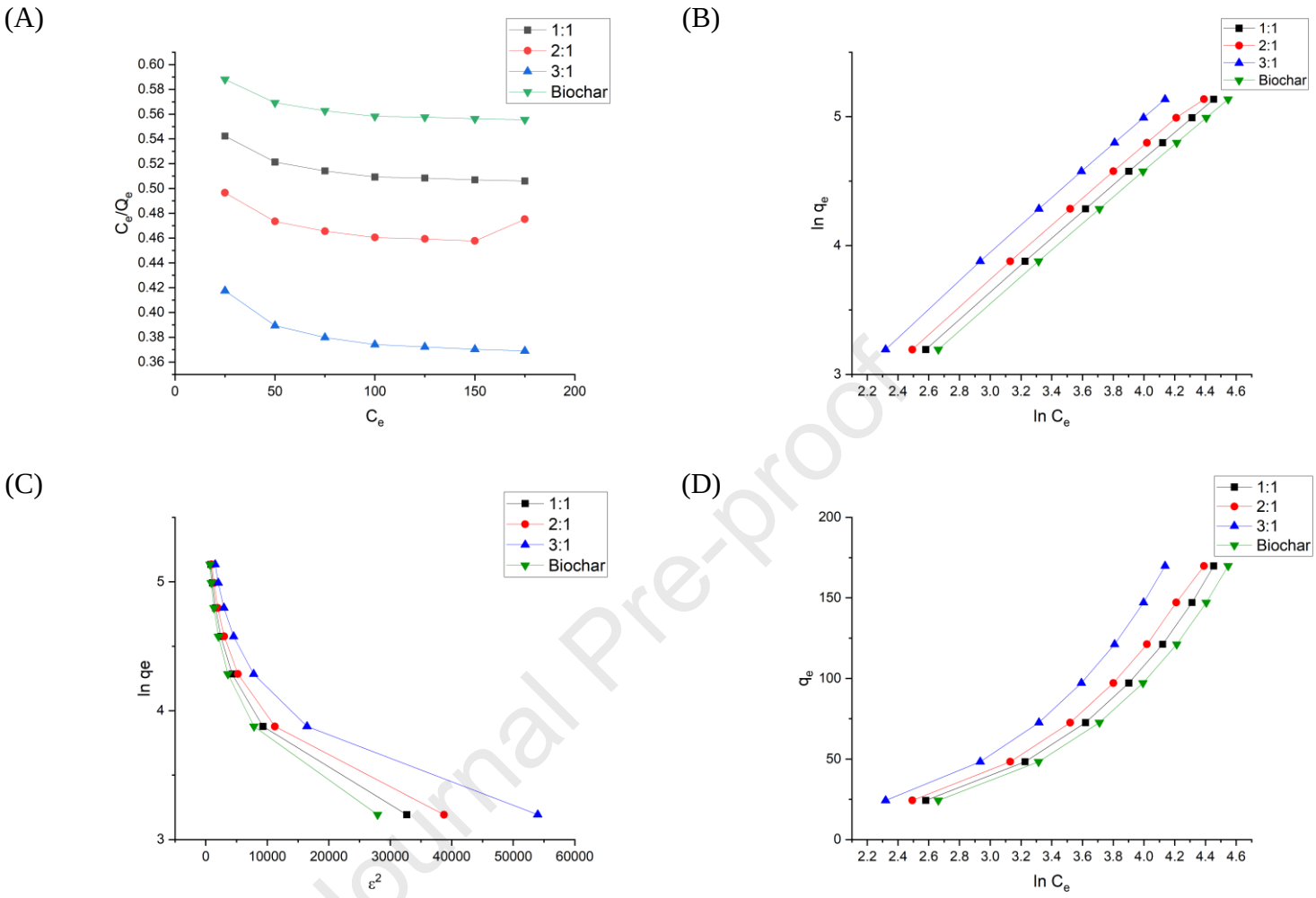

Figure 9 Plots of adsorption isotherm models:

(A) Langmuir, (B) Freundlich, (C) Dubinin-Radushkevich, and (D) Temkin

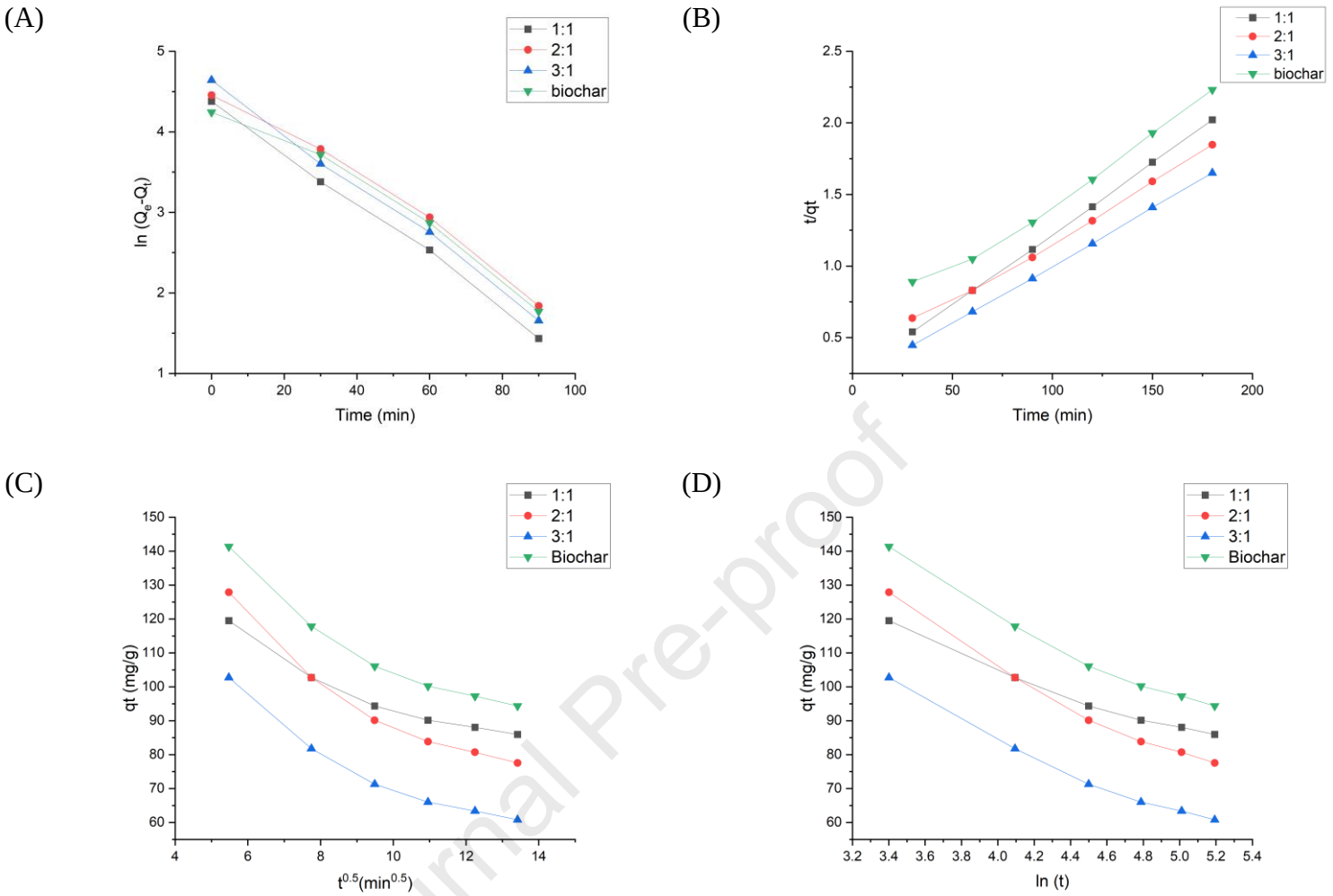

Figure 10 Plots of adsorption kinetics models:

(A) Pseudo-First, (B) Pseudo-Second, (C) Intraparticle Diffusion, and (D) Elovich

Declaration of interests

☒ The authors declare that they have no known competing financial interests or personal relationships that could have appeared to influence the work reported in this paper.

☐The authors declare the following financial interests/personal relationships, which may be considered as potential competing interests: